P- 46

DATA ANALYSIS AND INTERPRETATION RELATED TO SPACE SYSTEM/ENVIRONMENT INTERACTIONS AT LEO ALTITUDE

FINAL REPORT
NASA GRANT NAG3-792

Submitted to:

National Aeronautics and Space Administration
Lewis Research Center
Cleveland, Ohio 44135

By:

W. John Raitt
Robert W. Schunk
Utah State University Foundation
Logan, Utah 84322-9300

December 1991

Data Analysis and Interpretation related to Space System/Environment Interactions at LEO Altitude

Abstract

This report covers several studies made on the interaction of active systems with the LEO space environment experienced from orbital or sub-orbital platforms. The issue of HV-space interaction is covered by theoretical modelling studies of the interaction of charged solar cell arrays with the ionospheric plasma. The theoretical studies were complemented by experimental measurements made in a vacuum chamber by one of our collaborators. The other active system studied was the emission of effluent from a space platform. In one study the emission of plasma into the LEO environment was studied by using initially a 2-D model, and then extending this model to 3-D to correctly take account of plasma motion parallel to the geomagnetic field. The other effluent studies related to the releases of neutral gas from an orbiting platform. One model which was extended and used determined the density, velocity and energy of both an effluent gas and the ambient upper atmospheric gases over a large volume around the platform. This model was adapted to investigate both ambient and contaminant distributions around smaller objects in the orbital frame of reference with scale sizes of 1 meter. The other effluent studies related to the interaction of the released neutral gas with the ambient ionospheric plasma. An electrostatic model was used to help understand anomalously high plasma densities measured at times in the vicinity of the space shuttle orbiter. The importance of the chemical charge exchange process in this phenomenon led to a theoretical development of the collision term for chemical processes to be used in fluid models of the plasma interaction of the outgas with the ionosphere. The mechanism of the ionospheric ion /contaminant gas charge exchange interaction coupled with the rapid decline in neutral contaminant density on the ram side of the orbiting platform led to the development of a kinetic description of the contaminant ions in terms of an asymmetric ring distribution in velocity space. This was then coupled with a program developed to predict the output of a spherical retarding potential analyzer (SRPA) flown on two space shuttle orbiter flights for any ion distribution function to interpret unusual SRPA signatures observed on the shuttle flights in terms of a contaminant H_2O^+ ion distribution with the predicted asymmetric ring velocity distribution.

Introduction

The purpose of the research funded by the grant was to study the interaction of selected space systems with the space environment by computer modeling and by comparison with space measurements. The particular aspects of space systems which interact with the environment were ambient ionospheric interactions with high voltages, plasma clouds, and neutral gas release.

In general, new models were not completely developed under this grant, rather existing models were extended or adapted to apply them to realistic system-environment interactions for low earth orbit conditions.

The study of HV-ionosphere interactions concentrated on the use of a particle in cell (PIC) code to study the electric field configuration and current flux to a realistic geometry for a typical solar cell interconnect.

A plasma cloud interaction model was adapted to study the evolution of plasma density around a plasma jet emitting into the LEO environment. The model incorporated an ambient magnetic field and was configured to accommodate the very large ratio of flow velocities parallel and perpendicular to the magnetic field direction.

The neutral gas release studies had two components. The neutral gas model developed under other funding was run for typical space shuttle orbiter outgassing, flash evaporator and water dump efflux of water molecules at altitudes corresponding to low space shuttle orbital operations, intermediate altitudes and for altitudes similar to those anticipated for Space Station operations. In addition the model was adapted to study the interaction of smaller (meter sized) objects with the LEO environment including the effect of outgassing on the neutral environment around a simple geometry wake forming shield.

The interaction of the outgas cloud with the ionized component of the LEO environment was also studied. An earlier electrostatic interaction model studying the formation of H_2O^+ ions by charge exchange between contaminant H_2O molecules and the ambient ionospheric O^+ was adapted to incorporate the actual H_2O distribution predicted by the neutral environment model rather than use an assumed Gaussian distribution used by the earlier model. It became apparent that the scale size of the interaction region in the ram direction was comparable to the Larmor radius of the newly formed H_2O^+ ions. This prompted studies to develop a kinetic description of the contaminant ions which was needed to predict the response of an on board spherical retarding potential analyzer (SRPA) which was flown on two space shuttle flights. Comparisons of the expected kinetic distribution in the form of an asymmetric ring in velocity space, and the response of the SRPA were made and showed good agreement.

Finally, the neutral species model output was configured to provide an input to a code developed to predict the infrared excitation of the water molecules and their subsequent transport and de-excitation and emission of IR photons.

Solar Array Ionosphere Interactions

An important practical aspect of system-environment interaction for space platforms operating in the LEO altitude range is the interaction of the electric field developed at exposed interconnects of operational solar cell arrays needed to supply power for the systems on the platform. Depending on the particular platform, the potential difference between the platform ground and the interconnects may vary from ~30V for small unmanned vehicles to ~ 200V for large manned systems such as the Space Station. Existing studies have shown that the interaction with the greatest threat for electrical upsets occurs when the cell interconnects are at a negative potential to the ionospheric plasma. Under these circumstances electrical arc discharges have been observed to occur. Thus, depending on the amount of electrical charge in the arcing components, the electromagnetic interference caused by the current surge could exceed safety levels for some instruments.

As part of this study, theoretical particle in cell (PIC) codes were developed to simulate the actual geometry of the cell interconnects and calculate the electric fields resulting from different levels of biassing. This modeling work was supplemented by access to experimental data from Dr H. Thiemann, a collaborator based in Germany.

The PIC model takes advantage of the large number of identical solar cells in series connection. In such a configuration, there are small voltage gradients (~0.5 V) on each side of the cell, but these are negligible for the applied voltages considered in this study (100 and 250 V). With the repetition of the same geometry, the numerical scheme shown in Figure 1 concentrates on one solar cell unit with the conductive interconnector at the center of the bottom boundary. The processes occurring in the system are periodically repeated in the left and right directions. The grid system, for the identification of potential, electric field, and electron and ion densities at the grid points, uses a variable spacing with a higher resolution at locations close to the interconnector and the solar cell surface.

The following boundary conditions are applied to the potential and particles:

1) The lower boundary (y = 0) represents the solar cell surface with the exposed conductive interconnector in the center. The interconnector is biased to a prescribed positive potential ϕ_0. The cover glasses, as shown in Figure 1, are attached to the also biased grid fingers. In a vacuum, such a configuration creates surface potentials on the cover glasses of the order of the applied potential. A minor potential reduction associated with induced positive surface charges occurs because of polarization effects in the cover glass material. The corresponding boundary condition is given by the electric field discontinuity at the cover-glass grid points,

$$E^+ - \varepsilon E^- = \sigma_{ext}$$

where $\varepsilon(= 4)$ is the dielectric constant of the cover glass.

2) The upper boundary ($y=y_{max}$) describes the undisturbed plasma environment. We arbitrarily set the constant potential to zero, and this then represents the plasma potential,

$$\phi(x,y_{max}) = 0$$

3) The boundaries x = 0 and $x = x_{max}$ characterize the periodic boundaries simulating the already mentioned infinite repetition of the given particle and potential structures in the x-direction. These boundaries describe identical conditions with

$$\phi(0,y) = \phi(x_{max},y)$$

Plasma particles are treated in the following way. At the beginning of the simulation (t=0), the particles are uniformly distributed in the system to provide quasineutrality at the grid points of the system. Electrons and oxygen ions (the simulation used real ion masses!) are equipped with random velocities corresponding to typical ionospheric temperatures with Maxwellian features. Using a time-centered leapfrog scheme, the particles are advanced in time according to their inertia and the self-consistent electric fields. Particle tracking can result in the following interference with the boundaries. Particles hitting the interconnector

region contribute to the collected current. Particles impacting on the dielectric cover-glass surface contribute to the surface charge. In the assumed undisturbed plasma environment, near the upper boundary, particles are allowed to leave the system. New particles are supplied from the upper boundary to simulate a random thermal current from the ionospheric plasma. Particles leaving through the periodic boundaries are conserved. A particle crossing $x = x_{max}$ out of the system with the coordinates (x,y) is reintroduced to the system at $(x-x_{max},y)$. The corresponding velocity components do not change. An analogous scheme is applied for particles crossing the x= 0 boundary. The code also includes an option for secondary electron emission from the dielectric cover glasses.

Details of the model calculations can be found in Thiemann & Schunk (*1990*). In summary the calculations showed that PIC simulations could treat solar array/plasma interaction (sheath formation, surface charges and potentials, collected current, etc.) as a function of time for the biased solar array problem. For example, the study showed, for the non-emitting case, that there were three distinct regions on the cover glass that display different discharging features. Such a comprehensive picture had not been presented before.

Although realistic PIC simulations can be conducted, they do require substantial computer resources. For the simulations presented in this study the CRAY-XMP and CRAY-2 computers were used. The net CPU-time for a typical run of 200 plasma periods and the system size used was 6 h. Therefore, computer constraints limit the number of possible runs one can consider. In this study by Thiemann & Schunk (*1990*), simulations were conducted for both 100- and 250-V solar cells, an extended simulation domain, two solar cell thicknesses, and solar cells with secondary electron emission.

The simulations indicated that the sheath formation around interconnectors attached to high voltage solar arrays in an LEO plasma differs considerably from that predicted by Langmuir probe theory for the same voltage . The reason the simulation results differ from simple probe theory is because the complex material structure (plasma, conducting interconnector, dielectric cover glass) with different electrical properties influences the sheath formation. The combined action of interconnector shielding and dielectric discharging, both in competition with each other, results in perpendicular(to the solar cell) sheath dimensions that typically differ by one order-of-magnitude from simple probe theory. In the direction parallel to the solar cell, the difference is even larger. Without secondary electron emission from the cover glass, the perpendicular sheath radius and the current collected by the interconnector are directly related to the applied potential. However, with secondary emission, a planar potential structure forms in front of the interconnector and solar cells, and the interconnector current increases by a factor of 5 due to the collection of secondaries generated in the contact region of the solar cell.

One of the undesirable effects of the solar cell - environment interaction is the so-called "snapover" effect whereby large currents flow from to the interconnect when a threshold voltage has been exceeded. In the simulations involving secondary electron emission, the interconnector voltage was instantaneously applied, and hence, a planar potential structure existed at the beginning of the simulations. This potential configuration acted to accelerate the plasma electrons toward the cover glass, which in turn led to the production of secondary electrons. These secondary electrons then acted to maintain the planar potential structure and a quasi-steady state was quickly achieved. How this scenario relates to the snapover phenomenon is uncertain. For example, it is not clear if the same result would be obtained if the rise-time of the applied voltage is long compared to the electron plasma period so that individual sheaths could start to form before the applied

voltage increases beyond the snapover voltage. This whole issue of the transient development of HV sheaths in space plasmas is one which needs further consideration both by modeling and by experimental observations.

Measurements of leakage currents have been supported by the PIC code results [*Thiemann et al,* 1989], as have the appearance of arc discharges at different locations on a solar cell array [*Thiemann & Schunk,* 1990; *Thiemann et al,* 1990]

In order to obtain a better understanding of the transient phenomena resulting from the exposure of a HV-biased electrode to the unbounded ionospheric plasma, some of the support from this grant was directed to simulations of simpler geometries for the biased component than the solar cell.

One of the studies compared a PIC code result to a fluid model result for the transient development of the current to a sphere immersed in an unmagnetized plasma [*Thiemann et al,* 1990]. A major aim of this study was to verify the results of the fluid simulations and to determine whether or not plasma turbulence would be excited in the more rigorous PIC simulations. The first PIC simulations show that the plasma response predicted by both models are in qualitative agreement. In particular, it was possible to demonstrate that in both cases an electron density buildup occurs near the sphere, which later changed to a density depletion and a bump formation at a distance R = 30 from the sphere. The bump formation is related to the interaction of inflowing electrons with local ion density enhancements; which are possible once the ions are able to respond to the electric fields. The dynamic process leads to a potential double layer structure, which grows in time and propagates away from the sphere. At this moment, the computer requirements of the PIC-simulations prevent longer simulation run times. A continuation of the fluid simulation, however, showed a decay of the double layer as it moved outward .

The fundamental differences between both simulations are the oscillatory character of the electron density profiles, the structured ion density bump and the faster growth and decay character of the double layer structure for the PIC simulations.

In studying the density distribution of the electrons accelerated towards a biassed sphere, it has been observed experimentally and through modeling that the density increases in a toroidal region about the equator of the sphere in a plane perpendicular to the external magnetic field. The presence of this enhanced energetic electron flux holds the possibility of increased ionization in this toroidal region, and thereby producing additional plasma to enhance the current flow to a positively biased electrode in the ionosphere. A study of this effect was carried out partly under funding from this grant by *Ma & Schunk* [1991]

A fluid model was used to study the initial response of a magnetized, partially-ionized plasma to a positively biased high-voltage sphere. The model was based on a numerical solution of the time-dependent, three-dimensional, nonlinear fluid equations for ions and electrons and the Poisson equation. The main goal of the study was to determine the effect of impact ionization and collisions on the sphere-plasma interaction. The results of the study are relevant to a planned space and laboratory experiments. An example of the electron and ion densities resulting from the toroidal motion of the accelerated electrons and the ionization of neutral gas is shown in Figure 2. The results shown in the figure assumed an argon plasma with a density of 10^6 cm^{-3} and temperature of 0.1 eV, and a neutral argon density of 10^{13} cm^{-3}. The enhanced plasma density in the equatorial plane can clearly be seen.

Simulations were conducted for a sphere biased to +10,000 V embedded in Ar, O, N_2 and Ba plasmas. Different neutral densities and magnetic field strengths were also considered. From these simulations, the following conclusions were found:

1) When a high-voltage sphere is embedded in a magnetized, partially-ionized plasma, an electron density torus tends to form around the sphere in the equatorial plane at early times. The torus rotates about the sphere in the **E** x **B** direction. If the background neutral gas density is sufficiently high, the electrons accelerated by the strong electric fields associated with the sphere can ionize the gas by impact. At a critical ionization rate, a discharge or breakdown occurs. Collisions, on the other hand, act to decelerate the electrons and modify the space charge configuration (i.e. modify the toroidal shape).

2) For low Ar densities ($<5 \times 10^{11}$ cm-3), collisions and impact ionization are not important. The results are very similar to the collisionless plasma results obtained by Ma and Schunk (*1989b*).

3) For Ar densities of the order of 10^{12} cm-3, ionization occurs in the toroidal region where the electron density is elevated, but this impact ionization does not appreciably affect the current collection. In this case, a toroidal density configuration can be maintained without a discharge and the effect of collisions is to broaden the torus.

4) For Ar densities of the order of 10^{13} cm-3, the major ionization still occurs in a toroidal region. However, the ionization causes the plasma density and current collection to increase rapidly. A toroidal discharge is expected in this case.

5) For Ar densities of the order of 10^{14} cm-3, impact ionization occurs all around the sphere in an explosive manner. The discharge is likely to be spherical in this case.

6) The above results are for a magnetic field of 3 G. If the magnetic field is reduced and the other parameters are held fixed, the ionization that occurs tends to be more spherical. The current collection also tend to be higher.

7) Different molecules have different ionization energies, and collision and ionization cross-sections. Of the four species studied, Ar, N_2 and O have very similar properties, and hence, the features discussed above for Ar also apply qualitatively for N_2 and 0. However, barium behaves very differently. It has a larger collision cross-section and lower ionization energy. Therefore, for the same conditions, ionization and discharge processes are much easier to trigger in a Ba plasma. Also, compared to Ar, O and N_2, the density distribution, as well as the discharge, tends to be more spherical.

Plasma Contactor/Ionosphere Interactions

The interaction of plasma released into the ionospheric plasma at LEO altitudes has been studied for many years. The present study was used to partly support an aspect of this work which could have relevance to the directed release of plasma from a variety of systems including hollow cathode plasma contactors, plasma thrusters, MHD generators and other chemical release experiments.

Initially a 2-D model was developed to study the motion of a plasma cloud perpendicular to the geomagnetic field. The motion of artificial plasma clouds injected perpendicular to the geomagnetic field (B) in the ionosphere was studied using a time-dependent, two-dimensional, electrostatic model [*Ma & Schunk,* 1990]. Various geophysical and gas release conditions were considered, including different solar cycle, seasonal, and geomagnetic activity levels and different cloud sizes, injection velocities, release altitudes, and species. The effects of both magnetospheric electric fields and thermospheric winds on the cross-field motion were also considered. This systematic study led to the following conclusions:

1) initially, the newly created plasma clouds (Ba^+ and Li^+) move across B with the injected neutral clouds (for t< 1 s), but the ions are decelerated much faster than the neutrals and eventually become tied to the magnetic field;

2) at high altitudes (~400 km), the shape of a plasma cloud becomes long and narrow because it is formed via photoionization from the more rapidly moving neutral cloud. However, the precise cloud configuration and deceleration rate are determined by the ionospheric and release conditions;

3) the deceleration of plasma clouds is faster in summer than in winter, but the cloud Pedersen conductivities have similar magnitudes;

4) solar cycle and geomagnetic activity variations have a similar effect on the cross-field motion of plasma clouds. At solar maximum and high geomagnetic activity, the plasma clouds are decelerated faster and the cloud Pedersen conductivities are greater than at solar minimum and low geomagnetic activity;

5) at high altitudes, structure forms on the rear side of Ba^+ clouds in winter at solar minimum and low geomagnetic activity, but not for other geophysical conditions or for lithium;

6) the electrodynamic drift associated with the magnetospheric electric field acts to distort the shape of plasma clouds, change their direction of motion, and change their orientation relative to the neutral clouds;

7) at low altitudes (~ 200 km), the cross-field motion of both the plasma and neutral clouds is much slower, the cloud Pedersen conductivity is much greater (by two orders of magnitude), and the plasma cloud configuration is more isotropic than at high altitudes;

8) a thermospheric wind has an important effect on the cross-field motion of plasma clouds at 200 km, but its effect is small at 400 km. At low altitudes, the neutral wind acts to polarize the plasma cloud and eventually it moves in the direction of the thermospheric wind (a well-known result);

9) for high injection velocities and high cloud densities, the plasma cloud moves a greater distance across B and the cloud tends to become longer and narrower, particularly at high altitudes;

10) increasing the initial cloud size has an effect that is similar to lowering the cloud injection velocity;

11) if a cloud is partially ionized at the time of release, the motion of the initial ionization is affected by the electric field associated with the subsequent photoionization of the more rapidly moving neutral cloud;

12) comparing comparable barium and lithium releases, the lithium ion cloud has a lower Pedersen conductivity and is decelerated faster because of the lower photoionization rate and smaller mass for lithium.

The cloud slippage across **B** due to large injection velocities that are not field-aligned and the polarization effects associated with neutral winds were properly described with two-dimensional models, but in these cases the cloud dynamics along the magnetic field was neglected and the **B** field lines were assumed to be equipotentials. The quantities studied were either field line integrated densities or field line integrated conductivities. Since the conductivity along the **B** field is much larger than the perpendicular conductivity, the equipotential field line assumption should be reasonable over the scale of the plasma cloud. However, in order to verify such an assumption and to account for the dynamics of the cloud both along and perpendicular to the **B** field, a three-dimensional calculation is necessary.

A three-dimensional time-dependent model was developed to study the characteristics of a plasma cloud expansion in the ionosphere [*Ma & Schunk,* 1991]. The model makes it possible to use realistic ionospheric and cloud parameters. With the model the parallel and perpendicular motion of both the cloud and background ions can be studied. The electrostatic potential was solved in three dimensions taking into account the large parallel to perpendicular conductivity ratio. The model takes account of ion inertia, pressure gradients, the Lorentz force, the stress tensor (both collisional viscosity and the finite Larmor radius effect), Coulomb collisions and collisions between neutral and ionized species and the finite parallel conductivity.

Three sample simulations were considered: a plasma expansion of a nearly spherical 1 km Ba^+ cloud, both with and without a background neutral wind, and a long thin Ba^+ cloudlet. With or without the neutral wind the effective potential, which is different from the electrostatic potential if the electron temperature is included, is constant along the magnetic field for typical cloud sizes. The expanding plasma clouds become elongated in the magnetic field direction. The released Ba^+ ions push the background O^+ ions away

along the magnetic field as they expand. Consequently, a hole develops in the background O^+ distribution at the cloud location and on the two sides of the cloud O^+ bumps form. The entire three-dimensional structure, composed of the plasma cloud and the background plasma embedded in the cloud, slowly rotates about the magnetic field, with the ions and electrons rotating in opposite directions. An example of the elongated shape of a Ba^+ cloud initially released as a sphere after 40s is shown in Figure 3, and the depletion of the O^+ in Figure 4 for the same simulation conditions.

The cloud configuration takes the shape of a rotating ellipsoid with a major axis that expands with time. Perpendicular to the magnetic field, in the absence of the neutral wind the motion is insignificant compared to the parallel motion. With a neutral wind the motion along the magnetic field and the rotational motion are qualitatively unchanged, but the cloud and the perturbed background structure move in the direction of the wind, with a speed less than the wind speed. Perpendicular to the magnetic field the deformation of the cloud induced by the wind is characterized by steepening of the backside.

For an extended cloudlet along the magnetic field the potential is not constant along B. Also, the parallel expansion of the cloud and the snowplow effect are not important. The sheared rotational motion and diffusion act to smooth initial density perturbations on the cloud surface at early times, but later an instability develops that creates new density structures.

Neutral Outgas Cloud Interactions

The neutral model solves the Boltzmann equation

$$\frac{\partial f}{\partial t} + \mathbf{v}\cdot\nabla_{\mathbf{x}} f + \mathbf{a}\cdot\nabla_{\mathbf{v}} f = (\delta f/\delta t)_c$$

where $\nabla_{\mathbf{x}} f$ and $\nabla_{\mathbf{v}} f$ are the gradients of the distribution function with respect to position and velocity respectively, **a** is the acceleration due to external forces and $(df/dt)_C$ is the change in the distribution function caused by collisions between gaseous particles. The collision term is handled by the Krook collision term and external forces are neglected leading to a solution of the equations

$$\frac{\partial f_i}{\partial t} + v\cdot\nabla_x f_i = \sum_j \frac{f_{ij}' - f_i}{\tau_{ij}} + S_i$$

where i and j range over all interacting species, S_i is the explicit inclusion of contaminant gas sources,and t_{ij} is the fraction of gas particles that undergo collisions in unit time. The solution to the equation for the distribution function is obtained by a finite difference technique using a variable grid over the computational space with the smallest spacing around the source. By assuming symmetry about the spacecraft velocity vector and neglecting external forces, the problem is reduced to two dimensions--greatly reducing the computation effort required to obtain solution.

The coordinate system for position, $x=(r,z)$, is shown in Figure 5. The axis of symmetry is parallel to the vehicle velocity vector. The distance from the axis of symmetry, r, is always positive while the distance along the axis, z, may be positive or negative. The coordinate system for velocity space is similarly defined, $v=(v_r,v_z)$. Both v_r and v_z may be positive or negative. All coordinates, position and velocity, have their

origins at the orbiting vehicle. In this coordinate system, ambient gases have positive bulk velocity, v_z and no initial bulk velocity in the v_r direction.

Boundary conditions for position space are also shown in Figure 5. The boundary upstream is assumed to be unperturbed. This is always the case since it is far enough removed from the contaminant release point that significant perturbations never reach it. The two boundaries labelled constant are assumed to be equal to the adjacent interior grid point during each time step, *Dt*. They too are removed far enough that they have no detectable effect on results in the interior of the grid. The boundary labeled reflective is a result of the assumed cylindrical symmetry. The model needs only to solve from the axis of symmetry outward. A more comprehensive description of the neutral model has been published as a Ph.D. dissertation by *Thompson* [1989].

Simulation results are presented for the three sets of atmospheric parameters given in Table 1. The first two sets are representative of conditions during two space shuttle missions (OSS-1; Office of Space Sciences 1, March 1982: SL-2; SpaceLab 2, July 1985) and the third set are possible conditions for the proposed space station (SS). Number densities and temperatures of atmospheric species are obtained from the MSIS thermospheric model [*Hedin*, 1987]. These three cases cover a range of approximately 2 orders of atmospheric density. Only the major atmospheric constituents are considered. In the case of the higher altitude space station, atomic oxygen is dominant and so is the only atmospheric gas considered.

TABLE 1. Initial Atmospheric Parameters

	OSS-1	SL-2	SS
Vehicle	space shuttle	space shuttle	space station
Altitude (km)	250	320	450
n_{N_2} (m^{-3})	1.53×10^{15}	3.54×10^{13}	--
n_O (m^{-3})	2.81×10^{15}	2.35×10^{14}	3.20×10^{13}
T_{N_2} (K)	1300	900	1000
T_O (K)	1300	900	1000

In all cases the orbiting vehicle is simulated by a source of water moving at orbital velocity with respect to the ambient atmosphere. Water is used to as a contaminant since it is periodically dumped from the space shuttle and other manned vehicles as waste. Water is also used in the thermal control of the space shuttle, being released as vapor by the flash evaporator system (FES). Off gassing from shuttle surfaces is also a significant source of water [*Narcisi et al.*, 1983]. Results will be presented for various water source rates, but discussion will center about 10^{22} s^{-1} which is approximately that of the FES [*Pickett et al.*,1985].

The atmosphere is assumed to be initially isotropic in position and Maxwellian in velocity space. The water source is turned on suddenly at time equal zero and the model is allowed to run until steady state conditions are achieved in a region about the water source.

Steady state number densities of the modelled gases as they vary in position are plotted in Figures 6 through 10. Figures 6, 7 and 8 are for the OSS-1 set of conditions and a water release rate of $1x10^{22}$ s^{-1}. Each is composed of two main parts; a contour plot of the logarithm (base 10) of the number density of the species over a region of space around the water source and a surface plot of the same. The source is located at z=0, r=0 in the figures. The model results have been reflected about the axis of symmetry as a visual aid.

The density of water is shown in Figure 6. The density is highest at the source and falls off very quickly with distance. The fall-off is particularly rapid in the upstream direction since the incident atmosphere tends to strip back the expanding water cloud.

The densities of atomic oxygen and molecular nitrogen have very similar characteristics as seen in Figures 7 and 8. Note that the scale on the density axes in these plots are not the same and both are significantly different from Figure 6. The density of each species is enhanced near the water source due to collisions with the water cloud. These collisions transfer momentum from atmospheric gases to the water and decrease their velocities relative to the source. The densities of O and N_2 are sharply peaked within a radius of a few tens of meters about the source.

The density of H_2O is large enough within the region near the source at this release rate that most of the atmospheric particles are stopped and thermalized by the water. This results in the density depletion, or wake, behind the water source. The depletion shown is caused entirely by scattering of gases from the water cloud since the effects of vehicle surfaces are not included. The wake deepens with distance as the gases, heated by collisions, expand away faster than particles can fill in from the sides.

Figures 9 and 10 are results from the SL-2 set of initial conditions with a water release of $1x10^{22}$ s^{-1}. Note that the overall features of the density distribution are similar to the OSS-1 case except for the larger spatial scale. The peak density shown is significantly smaller than that predicted for the OSS-1 conditions. This is due to the larger grid spacing near the source used for this case; Dr=Dz=500 m compared with Dr=Dz=50 m for OSS-1. Though the contaminant water is released at a constant rate of 10^{22} s^{-1} in both cases, it is released into a larger cell in the SL-2 case. Effectively, the cloud is averaged over the larger grid cell, thereby reducing the computed peak density.

When the same grid spacing used in the OSS-1 case (Dr=Dz=50 m) is used for the SL-2 and SS cases, the peak H_2O density is slightly higher at the higher altitudes. This is directly attributable to the combination of lower density and lower mean mass of the ambient gases at the higher altitudes. Since the atmosphere cannot deliver as much momentum and energy to the water cloud, the atmosphere is less able to strip the water back away from the source. Peak water densities for the various initial conditions obtained with identical grid spacings are given in Table 2.

TABLE 2. Peak H_2O Densities (m^{-3})

Dump Rate (s^{-1})	OSS-1	SL-2	SS
10^{21}	1.42×10^{16}	2.73×10^{16}	3.67×10^{16}
10^{22}	1.21×10^{17}	3.83×10^{17}	4.07×10^{17}
10^{23}	3.43×10^{18}	4.05×10^{18}	4.81×10^{18}

The spatial size of the water cloud for the various sets of conditions is summarized in Tables 3 and 4 Table 3 lists the distance from the source to the position in space where the density of water falls to a specified value for all three outgassing rates. Table 4 lists the same information as Table 3 for the SL-2 and SS cases for 1×10^{22} s^{-1} outgassing. Note that the cloud is much larger for the higher altitude cases.

TABLE 3. Spatial Dimensions of the Water Cloud for the OSS-1 Set of Conditions and Various Source Rates in the Upstream, Radial and Downstream Directions

Dump Rate (s^{-1})	1×10^{16}			1×10^{15}			4.37×10^{15}		
	-z	r	+z	-z	r	+z	-z	r	+z
10^{21}	<25	<25	31	63	75	225	235	320	1700
10^{22}	57	65	349	243	375	3400	567	1000	*
10^{23}	238	283	861	494	710	*	905	*	*

* not achieved in modelled space

The time evolution of the density of each species can be tracked at each point in space. Figure 11 shows the density at three locations (500 m upstream, 500 m downstream and at the source location) of H_2O and the sum of O and N_2 for the OSS-1, 1×10^{22} s^{-1} case. Note that the density axis for the H_2O plot is logarithmic while that for O and N_2 is linear. The density of each gas quickly achieves a steady value near the source. Away from the source no change is initially seen in any of the species since the sourced water molecules must travel the intervening distance at finite velocity. The densities of O and N_2 show only slight enhancement upstream from the source. The density of these atmospheric species downstream falls to a minimum shortly after the effects of the released H_2O are seen and then rises slowly to a steady value. The wake is deeper at short times

since the atmospheric gases, which were slowed by collisions at the water source, have not had time to traverse the intervening distance at their new, slower velocity. As conditions reach steady state, those particles which were slowed by collisions have travelled from the source location and partially fill the void. The density is somewhat decreased from ambient even in steady state since the gases were heated as well as slowed and hence are expanding away in all directions.

TABLE 4. Spatial Dimensions of the Water Cloud for the SL-2 and SS Sets of Conditions in the Upstream, Radial and Downstream Directions for a Source Rate of $1x10^{22}$ s^{-1}

	$1x10^{16}$			$1x10^{15}$			$1x10^{14}$		
	-z	r	+z	-z	r	+z	-z	r	+z
SL-2	212	222	557	725	820	1480	3250	4750	*
SS	297	328	407	2350	2410	*	7000	8000	*

* not achieved in modelled space

When the source of water molecules is turned off, collisions with the atmospheric gases causes the H_2O density in the vicinity of the source location to fall off quickly with time. This can be seen in Figure 12 which is a plot of the density of water averaged over a 1 km square centered on the source, for each altitude as a function of time after termination of the water source. Symbols are shown in Figure 12 where the density of water is equal to the ambient atmospheric density for each altitude. The density of H_2O is relatively slow to decay for the highest altitude, taking about 9 s to reach ambient levels. In contrast, the density fall off is very abrupt for the low altitude case where the water density falls below ambient in less than 0.1 s.

The reduction of water density at the source location is the result of two processes; the dispersion of the water cloud by expansion and the acceleration of the cloud away from the source by collisions with the incident atmosphere. This can be seen in Figure 13 where the density of H_2O at the source location and at the location of the highest H_2O density on the grid are plotted as functions of time. Initially and for approximately one second after termination of the contaminant water, the cloud peak and source are essentially coincident within the 1 km^2 cell. During this time, the water density falls off primarily because those molecules which leave the vicinity of the source due to their thermal velocities are not replaced by the source. After this time however, the density at the source falls off more quickly than simple expansion as the cloud is accelerated, as a body, away from the source. Though the peak density of the cloud is significant after even 10 s the density at the source location has fallen to less than $1x10^{12}$ m^{-3}.

The velocity distribution functions predicted by the numerical model frequently vary considerably from Maxwellian distributions. Therefore, it is not possible to fully assess

the solutions obtained by observing the low-order integrated moments alone. Also, it is difficult to interpret the values of the low-order moments such as velocity and temperature for non-Maxwellian velocity distributions.

The velocity distributions of the interacting gases are approximately Maxwellian downstream from the source near the axis of symmetry, it is possible to interpret the calculated velocity and temperature moments. Figure 14 shows the density, bulk velocity magnitude and temperature of the gases along the axis of symmetry. All gas species are moving relatively slowly (~2 km/s) near the source and are accelerated to the velocity of the ambient atmosphere by the onrushing atmospheric particles with time. O and N_2 are shown having a slightly higher velocity than H_2O. This is a result of the filling in of unperturbed atmospheric particles mentioned previously. The large populations of all the gases are moving at nearly the same velocity. However, when the relatively small number of unperturbed particles, which have velocities greater than the thermalized population, are included in the integration to calculate bulk velocity, their contribution significantly increases the result. The bulk velocity of water does not show this effect since the ambient density of H_2O is zero.

The temperature of H_2O shows a slow increase with distance from the source as it is heated by collisions with atmospheric particles. After reaching a peak approximately 1500 m downstream from the source, the temperature of H_2O begins to decrease toward ambient levels as expansion begins to dominate heating by collisions. The effects of filling by unperturbed particles in even more pronounced in the temperature of the ambient gases as seen if Figure 14. The main population of each gas has a temperature nearly that of H_2O, but the inclusion of unperturbed particles in the integration doubles the calculated temperature in the region near the source.

Upstream from the source the calculated temperatures reach values exceeding 10,000 K. This is the result of non-Maxwellian velocity distributions for the gases in this region of space and is not indicative of a heated, thermalized population. The bulk velocity of O and N_2 are also misleading upstream from the source. The curve shown is the weighted average of both unperturbed and scattered populations, not the velocity of a single Maxwellian.

By using the results obtained with the coarse grid discussed previously as initial/boundary conditions, the model can zoom in to much finer spatial resolutions. Also, the effects of simple physical structures can be included. Figures 15 and 16 show results obtained using this procedure for the OSS-1 ambient conditions and an outgas rate of $1x10^{21}$ s^{-1}. In Figures 15 and 16 a wall with radius of 3 m is located at the origin of the coordinate system. Gas particles incident on the wall are elastically scattered. A deep wake is induced immediately behind the wall. However, the wake is not as deep as that which would occur if no contaminant gas were present. Significant amounts of both ambient and contaminant gases are scattered by collisions within the relatively dense water cloud, filling the wake.

The depth of the wake is found to be dependent on both altitude and the rate of water release. Figure 17 is a plot of the total neutral density (both ambient and contaminant) along the axis of symmetry, which passes through the middle of the wall, for various outgas rates. Note that for the highest outgas rate, the total neutral density behind the wake forming wall is still above ambient levels. Figure 18 shows the density variation in the radial direction just behind the wall. The position of the edges of the wall are indicated by vertical lines.

The dependence of the filling of the wake on altitude can be seen in Figure 19. Note that even though the density of the water at the source location is essentially the same for the two altitudes, the filling behind the wall is reduced by approximately a factor of 10 at the higher altitude. The filling rate does not display a one-to-one with either altitude nor outgas rate. Further modelling will need to be done before the quantitative dependence can be determined.

Electrostatic Plasma Interaction Model

Early results from the use of a thermal ion plasma probe on the space shuttle showed that the ions measured often had a greatly differing distribution function from that expected from the ambient ionospheric population (*Banks et al, 1987*). In particular the data indicated that the ion density increased considerably over ambient ionospheric values, and there was also evidence of the presence of ions of greater relative energy that the ambient O^+ ions(*Raitt et al, 1984; Siskind et al, 1984*). Information on the outgas rates, and early measurements of the gas pressure in the vicinity of the orbiter showed that the pressure was far too low for photo ionization to be effective at producing the densities observed, and chemical effects such as charge exchange could only maintain the same ion density unless dynamic effects were also present. In an attempt to understand the nature of the contaminant ions, work was commenced on an electrostatic model for the interaction of the ambient ionospheric ions with outgassing or released contaminant gases from the orbiter.

A two-dimensional, finite-difference model was used to solve for the time evolution of low beta plasma within the neutral contaminant cloud in the vicinity of space platforms in low earth orbit. The model of the ambient and contaminant plasma dynamics takes into account the effects of the geomagnetic field, electric fields, background ionosphere, ion-neutral collisions, chemistry, and both Pedersen and Hall currents. Net ionization and charge exchange source terms are included in the fluid equations to study electrodynamic effects of chemistry within a moving neutral cloud in the low earth orbit ionosphere. The model was then used with complete water cloud chemistry to simulate the known outgassing situation of the space shuttle Orbiter(*Eccles et al, 1989*).

The set of equations used within the model was developed using the following assumptions:

1) It was assumed that the plasma could be described as a fluid. This assumed that randomizing rates were high enough to maintain near Maxwellian distributions. This is a severe restriction and is possibly violated by the plasmas within a dense outgas cloud. The dominant collision within a water-vapor outgas cloud drives the H20+ to a nonthermal distribution. However, Raitt et al. (*1984*) describe the contaminant ion signature they observed as having a broad distribution suggesting randomizing collisions had occurred and the fluid approximation was justifiable.

2) It was assumed that the plasma was quasi-neutral This assumption was justified by the comparison of scale lengths of interest (~100 m) to the Debye length of the plasma (~1 cm).

3) It was assumed that the plasma was a low beta plasma. The comparison of plasma motional energy and the energy of the geomagnetic field reveals a worst case beta of 0.01 ($n_{H20+} = 10^{13}$ m-3, $V_{H20+} = 7700$ m/s, $B = 0.5 \times 10^{-4}$ Wb/m2)

4) It was assumed that the plasma perturbation did not affect the ambient and contaminant neutral bulk properties. For the time scales modeled (~ 0.2 s) the chemistry and collisions between the plasma and neutral components within the model will not change the neutral parameters.

A contaminant cloud of a single generic species, G, was used to investigate the characteristics of different ionosphere-outgas interactions. The neutral cloud is modeled by a Gaussian density profile traveling at orbital velocity perpendicular to the magnetic field (stationary frame of reference).

$$n_G(r) = n_{Gmax} \exp(-r^2 / r_0^2)$$

$$U_G = 7700 \text{ m/s}$$

The Gaussian density profile provides neutral cloud parameters, n_{Gmax} and r_0, which can be varied in order to investigate resulting plasma density profiles and motions. This is an oversimplification of the neutral cloud. It was chosen primarily for the stability it provides in the numerical technique used. For a freely expanding neutral cloud formed by a point source, the density would vary as $1/r^2$. However, the space platform and the cloud of ice crystals that form during water dumps can provide an extended outgassing source and the cloud would follow $1/r^2$ only at great distances from the extended source. Therefore within this study the qualitative aspects of the neutral contaminant-ionospheric plasma interactions were emphasized using a simplified description of the gas cloud density around the Orbiter which nevertheless retains those gross characteristics which are important to the electrodynamics of the plasma [*Thompson and Raitt,* 1987; *Eccles and Raitt,* 1987]. The physical situation being modeled is shown in Figure 20.

The neutral gases will interact with the ambient solar UV flux, and with the ambient ionospheric plasma through reactive and elastic collisions. For photoionization and other ionizations that depend only on the neutral density,

$$G \rightarrow G^+ + e$$

For charge exchange,

$$O^+ + G \rightarrow G^+ + O$$

A comparison was made of the model results with plasma observations made during daytime on OSS-1/STS-3 mission. The enhanced densities observed by the ion probe could only attained by a generic chemistry model if a net ionization rate 1000 times higher than the photoionization rate of water was used. It was also shown that significant plasma buildup at the front of the contaminant neutral cloud can occur due to momentum

transfer from the neutral outgas cloud to the plasma through elastic collisions and charge exchange.

The currents caused by elastic and reactive collisions result in the generation of a small polarization electric field within the outgas cloud. The polarization electric field, in combination with the geomagnetic field, causes the plasma to drift with the contaminant neutral cloud but at a slower speed in the stationary reference frame. The slow drifting in the Orbiter frame is consistent with OSS-1 plasma probe interpretations where a high relative speed between the Orbiter and ions is inferred. Also, if there is a fast net ionization process within the outgas cloud, the drifting plasma allows for nonlinear buildup of plasma density with respect to the net ionization rate. Detailed plots of the ionospheric and contaminant plasma distributions together with the polarization electric fields are presented in *Eccles [1988]* and *Eccles et al [1989]*.

It was clear that the chemistry of the charge exchange reactions played the major role in determining the outgas/ionosphere interaction for a platform in low earth orbit. Part of the work under this grant was an extension of the earlier work by Eccles et al to formulate the reactive collision term in a general way to enable it to be incorporated directly in the Boltzmann equation, or in fluid equations derived from the Boltzmann equation [*Eccles & Raitt*, 1991].

The Bhatnagar-Gross-Krook (BGK) technique of reactive collisions for fluid theory was expanded for use in general fluid and plasma physics. Reactive collision terms were developed for kinetic and transport theory for any level of moment approximation. The reactive collision terms for the 13-moment approximation were derived with the assumptions; 1) all reactants and products have 13-moment distribution functions, 2) simple, classical assumptions provide sufficient models for reaction dynamics, 3) the reaction rate is energy independent. The resulting 13-moment collision terms are appropriate to be used in non-equilibrium flow environments; i.e. where the reactants and products of reactions have large differences in temperature or velocity and/or have non-Maxwellian distributions. The clarification of the manner in which assumptions are introduced allows the BGK reactive collision technique to be used for development of any reaction. Important considerations for correct use of the BGK reactive collision method are discussed in the context of space plasma environments involving the emission of contaminant gas species from space platforms operating in the LEO altitude range.

Observation of Ion Ring Velocity Distributions

As the O^+ ions in the ambient plasma pass through the water cloud surrounding large spacecraft some will undergo a charge-exchange reaction with the neutral water . These newly created H_2O^+ ions have a large average velocity relative the the geomagnetic field and, as they gyrate about the magnetic field, form a ring distribution in velocity space.

The production rate of the water ions is directly proportional to the number density of the neutral water. So, using the neutral density profile obtained from the neutral mode previously discussed, the production rate of H_2O^+ as a function of time and position relative to the water source can be calculated. The water cloud density is sharply peaked at the source location and falls off very rapidly in the upstream direction, therefore, the highest H_2O^+ production rate is also at the source.

The distance travelled by a spacecraft at orbital velocity in one ion cyclotron period is larger than the spatial scale size of the water cloud. So, ions produced near the water source, where the production rate is the highest, do not have time to gyrate even one complete revolution before the spacecraft moves beyond their trajectory. The result is an asymmetric ring distribution in velocity space, as shown in Figure 21.

We have written a simple model that calculates the velocity distribution function of the total plasma (both O^+ and H_2O^+) as a function of position relative the source of water vapor. No transport mechanisms or wave-particle interactions are considered in this model. Results from the model are scaled into the same units as measured ion distributions obtained using the SRPA. Figure 22 is a plot of predicted and measured ion signatures for similar conditions. The broad peak centered at approximately five volts is the contribution from the ambient O^+. The smaller peak near zero volts is the contribution from the H_2O^+ population with the calculated asymmetric velocity-distribution function. Note that the curves agree very well except that the trough between the two peaks is partially filled in the measured data. It is thought that this filling is due to collisions between ions and perhaps wave-particle interactions collapsing the ring distribution to a Maxwellian.

Summary

We have studied aspects of space system /environment interaction at LEO in two principal areas; HV-ionosphere interaction and effluent-upper atmosphere interaction. The HV-ionosphere interaction studies included solar cell array interactions at different bias levels, and simple geometry interactions of a HV biased sphere including the effect of the geomagnetic field and the residual neutral gas in the vicinity of the sphere. The effluent interaction included plasma releases, fully allowing for the effect of the external geomagnetic field, and outgas-upper atmosphere interactions. The latter interactions described the distribution of effluent neutral gas around an orbiting platform, and also the change to the ionization density as a result of the interaction of the outgas cloud with the ambient ionosphere.

The PIC code simulations of the solar cell-ionosphere interaction model showed that the plasma sheath formed around exposed metallic interconnects was considerably different than that predicted by Langmuir theory. The complex surfaces around the interconnections act to distort the sheath by the effects of secondary emission from the dielectrics present and consequent surface charging effects. The model is able to compute the electric field configuration and intensity showing locations of field concentrations. The code also allows current collection profiles to the interconnect to be computed. In the absence of secondary emission, the currents show a sub μS rise time to a peak followed by a similar time constant decay to a steady state value. When secondary emission is present the current rapidly rises to a value about four times that seen without secondary emission, and then shows a constant, but noisy, level.

The extension of the HV-ionosphere interaction to evaluate the transient response of biassed spheres showed encouraging results using a 3-D time dependent non-linear fluid code. The formation of a toroidal region of orbiting electrons **E X B** drifting under the combined effects of the **E**-field generated by the sphere bias, and the geomagnetic **B**-field agrees well qualitatively with experimental observations where this phenomenon is visualized by enhanced ionization in the torus, and other modelling studies using much more computer intensive particle codes.

The plasma effluent cloud interaction code was evolved from a 2-D code to study cross B-field transport of the plasma effluent to a fully 3-D fluid code to study the full spatial morphology of the cloud after it had been released.The expected elongation of the cloud along the **B** direction was modeled, and a rotation of the cloud about the longitudinal axis of the ellipsoid was predicted. The expanding cloud also caused a depletion of the ionospheric O^+ ions in the center of the cloud with an enhancement at the sides to which the O^+ ions are pushed by the contaminant ions. As time progresses the model predicts the formation of instabilities which develop new density structures.

Neutral gas release studies were extended by using a previously developed code which addressed the question of the distribution of outgas or dumped gas around an orbiting platform. The studies were extended to show the distribution of the contaminant and ambient atmospheric gases on a spatial large scale at a range of altitudes up to those at which the Space Station is expected to operate. In particular the time evolution of the enhanced neutral density for onset and stopping of the contamination was studied. We found that the contaminant gas took times of the order of tenths of seconds after turn-on to build up at 100's meters from the orbital platform, and decayed in times of 1-10 sec depending on the altitude of the platform. In order to investigate the contaminant around structures sized to match that of large solar cell arrays, the neutral gas code was adapted to model the gas parameters around meter sized objects. It was found that a the lower altitude levels, typical shuttle flash evaporator emission rates could fill the wake of a solid object to a density equalling that of the undisturbed atmospheric density at that altitude.

Finally the work on the interaction of a neutral contaminant cloud was extended to attempt to predict the response of an ion probe flown on two space shuttle flights. This proved to be impossible without extending the neutral gas ionosphere interaction to predict the velocity distribution of the contaminant ions formed by charge exchange. In turn this distribution could be used with a code developed to predict the ion probe response to any distribution rather than the assumed Maxwellian which had been used previously. This comparison showed good agreement with the predicted contaminant ion distribution and enables us to use the ion probe response as an indicator of the properties of the non-Maxwellian contaminant ions that exist close to their generation region near the platform. In an attempt to improve the fluid code as a means of predicting contaminant ion properties, a general development was undertaken to formulate the collision term in the Boltzmann and thence fluid equations to correctly take account of chemical rather than collisional interactions.

Acknowledgements

We ackowledge the invaluable assistance provided to these studies by our colleagues, Dr. J. V. Eccles, Dr. H. Thiemann, Dr.T.-Z. Ma, and Dr. D. C. Thompson.

References

Banks P. M., W. J. Raitt , P. R. Williamson, A. B. White and R. I. Bush; Results from the vehicle charging and potential experiment on STS-3, J.Spacecraft & Rockets, *24*, 138-149, 1987

Eccles J. V., The electrodynamics of plasma within the outgas cloud of the space shuttle orbiter; PhD dissertation, Utah State University, 1988

Eccles J V.., W. J. Raitt ,The effect of plasma electrodynamics on the chemistry within the outgas cloud of the space shuttle orbiter; EOS Trans. AGU, *68*, 1399, 1987

Eccles J V.., W. J. Raitt and P. M. Banks, A numerical model of the electrodynamics of plasma within the contaminant gas cloud of the space shuttle orbiter at LEO, J. Geophys. Res., *94*, 9049-9064, 1989

Eccles J V.., W. J. Raitt , Reactive collision terms for fluid theory; Planet. Space Sci., In press, 1991

Hedin, A. E., MSIS-86 thermospheric model, J. Geophys. Res., *92*, 4649, 1987.

Ma T.-Z. and R. W. Schunk, A fluid model of high voltage spheres in tthe ionosphere; Planet. Space Sci., *37*, 21, 1989

Ma T.-Z. and R. W. Schunk, Ionization in the magnetized ionosphere surrounding a high voltage sphere; Planet. Space Sci., In Press 1991

Narcisi, R., E. Trzcinski, G. Federico, L. Wloydka and D. Delorey, The gaseous and plasma environment around the space shuttle, paper presented at Shuttle Environment and Operations Meeting, AFGL-TR-83-2659, American Institute of Aeronautics and Astronautics, New York, 1983.

Pickett, J. S., G. B. Murphy, W. S. Kurth, C. R. Goertz and S. D. Shawhan, Effects of chemical releases by the STS-3 orbiter on the ionosphere, J. Geophys. Res., *90*, 3487, 1985.

Raitt W. J. , D. E. Siskind, P. M. Banks and P. R. Williamson, Measurements of the thermal plasma environment of the space shuttle; Planet. Space Sci., *32*, 457-467, 1984

Siskind D. E., W. J. Raitt , P. M. Banks and P. R. Williamson,Interactions betwen the orbiting space shuttle and the ionosphere; Planet. Space Sci., *32*, 881-896, 1984

Thiemann H. and R. W. Schunk, Particle-in-cell simulations of sheath formation around biassed interconnectors in a low-earth-orbit plasma; J. Spacecraft and Rockets, *27*, 554-562, 1990

Thiemann H., R. W. Schunk and L. Gerlach, Solar arrays in the LEO-plasma environment: a model for leakage current phenomena deduced from experimental and theoretical studies; Proc. ESA SP-294, 809-813, 1989

Thiemann H., R. W. Schunk and K. Bogus, Where do biased solar arrays arc?; J. Spacecraft and Rockets, *27*, 563-565, 1990a

Thiemann H., T.-Z. Ma and R. W. Schunk, High voltage spheres in an unmagnetized plasma: Fluid and PIC simulations; Adv. Space Res. 1990b (In press)

Thompson, D. C., A Numerical Model of the Interaction of Contaminant Neutral Gases Released from Orbiting Spacecraft with the Ambient Terrestrial Atmosphere, Ph.D. dissertation, Utah State University, 1989.

Thompson D. C. and W. J. Raitt, The interaction of neutral contaminant gases introduced by torbiting spacecraft with the ambient terrestrial atmosphere; EOS Trans. AGU, *68*, 1399, 1987

Figure captions

Fig. 1 Simulation grid for solar cell model

Fig. 2 Electron and ion densities in a meridian plane of a sphere charged to 10kV in the presence of a magnetic field of 3G

Fig. 3 Barium ion plasma cloud density distribution (logarithmic) in planes containing (upper panel) and perpendicular (lower panel) to the geomagnetic field, 40 sec after plasma release.

Fig. 4 Ionospheric oxygen ion density distribution (logarithmic) in planes containing (upper panel) and perpendicular (lower panel) to the geomagnetic field, 40 sec after plasma release.

Fig. 5 Boundary conditions and coordinate layout in position space.

Fig. 6. The density of water for the OSS-1, $1\xi 10^{22}$ s^{-1} case as a function of position.

Fig. 7. The density of atomic oxygen for the OSS-1, 1×10^{22} s^{-1} case as a function of position.

Fig. 8 The density of N_2 for the OSS-1, 1×10^{22} s^{-1} case as a function of position.

Fig. 9. The density of water for the SL-2, 1×10^{22} s^{-1} case as a function of position.

Fig. 10. The sum of the densities of atomic oxygen and molecular nitrogen for the SL-2, 1×10^{22} s^{-1} case as a function of position.

Fig. 11. The time variation of the densities of the modelled gases at three locations: r=0, z=-500; r=0, z=0 and ; r=0, z=500, for the OSS-1, 1×10^{22} s^{-1} set of conditions.

Fig. 12. Contours of the size of the water cloud as it varies in time for the OSS-1, 1×10^{22} s^{-1} case. Each contour encircles that region of space where the density of water is greater than the density of the ambient atmosphere. The innermost contour is at 0.01825 s and subsequent contours occur at 0.01825 s intervals.

Fig.13. The decay of the density of water in time at the source location after the source has been turned off for the three modelled altitudes.

Fig.14. The densities, velocity magnitudes and temperatures of the interacting gases for the OSS-1, 1×10^{22} s^{-1} case along the axis of symmetry. The gray areas are those regions of space where highly non-Maxwellian distributions are predicted.

Fig.15. The number density of H_2O in the vicinity of a small elastic plate.

Fig.16. The sum of the number densities of O and N_2 in the vicinity of a small elastic plate.

Fig.17. The total number density along the axis of symmetry at 250km for various outgas rates in the vicintiy of a small elasitc plate.

Fig.18 The total number density perpendicular to the axis of symmetry at 250km for various outgas rates just behind a small elastic plate.

Fig.19. The total number density along the axis of symmetry at 250km and 320km for a water outgas rate of 10^{22} s^{-1} in the vicinity of a small elastic plate.

Fig.20. Schematic diagram of the physical situation modeled and the polarization field (E_p) resulting from the motion of the newly created contaminant ions relative to the geomagnetic field (B_0)

Fig.21. An asymmetric ring velocity distribution due to charge exchange between O^+ and H_2O.

Fig.22. The calculated (smooth curve) and measured response of the SRPA to a plasma composed of ambient Maxwellian O^+ and contaminant asymmetric-ring distribution H_2O^+ ions.

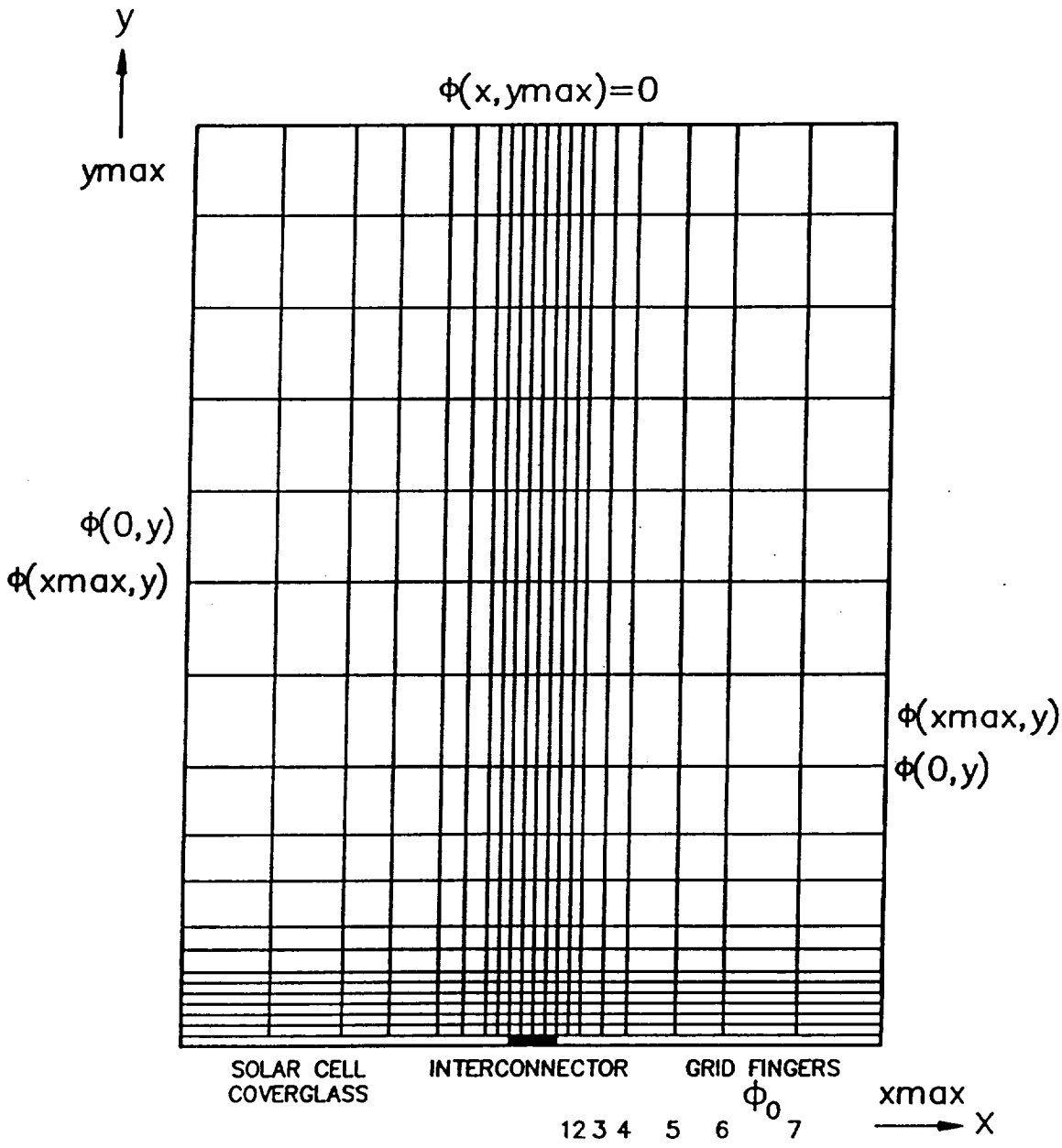
y
Φ(x,ymax)=0
ymax
Φ(0,y)
Φ(xmax,y)
Φ(xmax,y)
Φ(0,y)
SOLAR CELL
COVERGLASS
INTERCONNECTOR
GRID FINGERS
Φ_0
xmax
X
1 2 3 4 5 6 7

Figure 1.

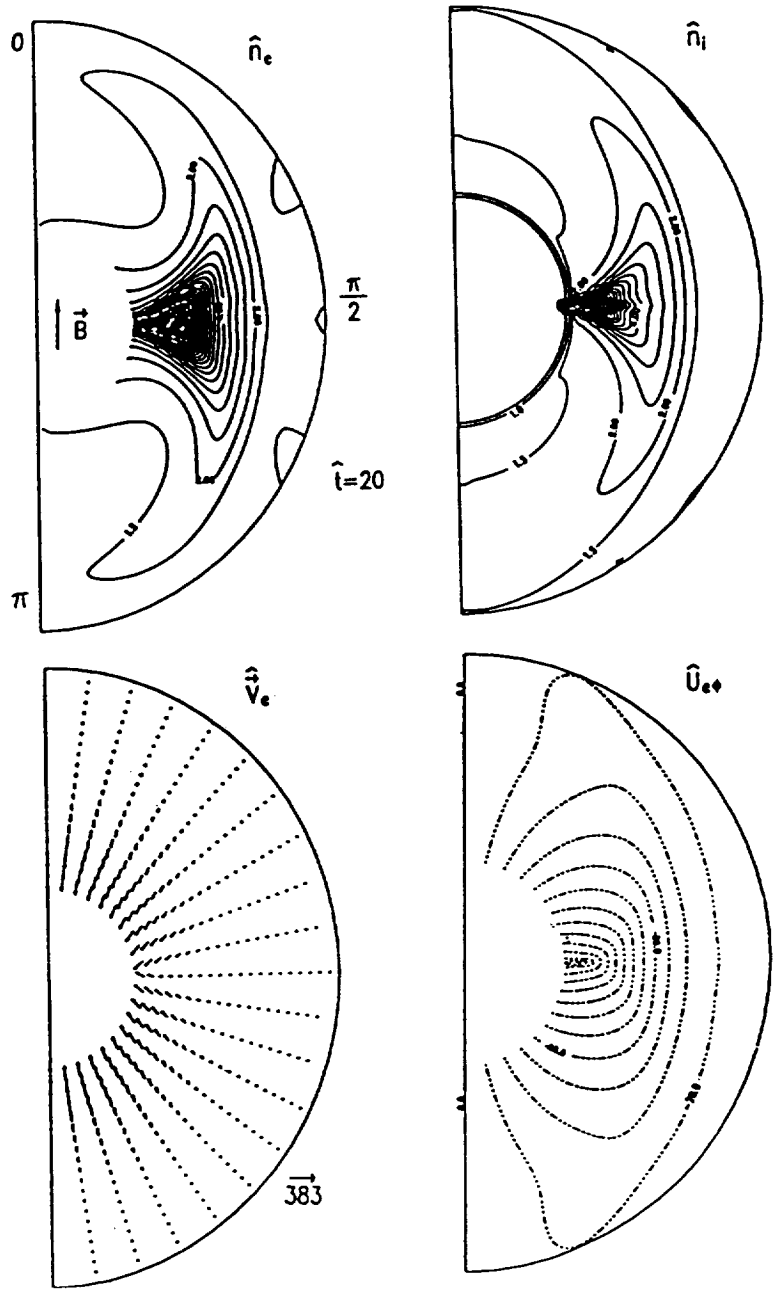
0
$\hat{n}_e$
$\hat{n}_i$
$\vec{B}$
$\frac{\pi}{2}$
$\hat{t}$=20
π
$\hat{\vec{V}}_e$
$\hat{U}_{e\phi}$
$\overrightarrow{383}$

Figure 2.

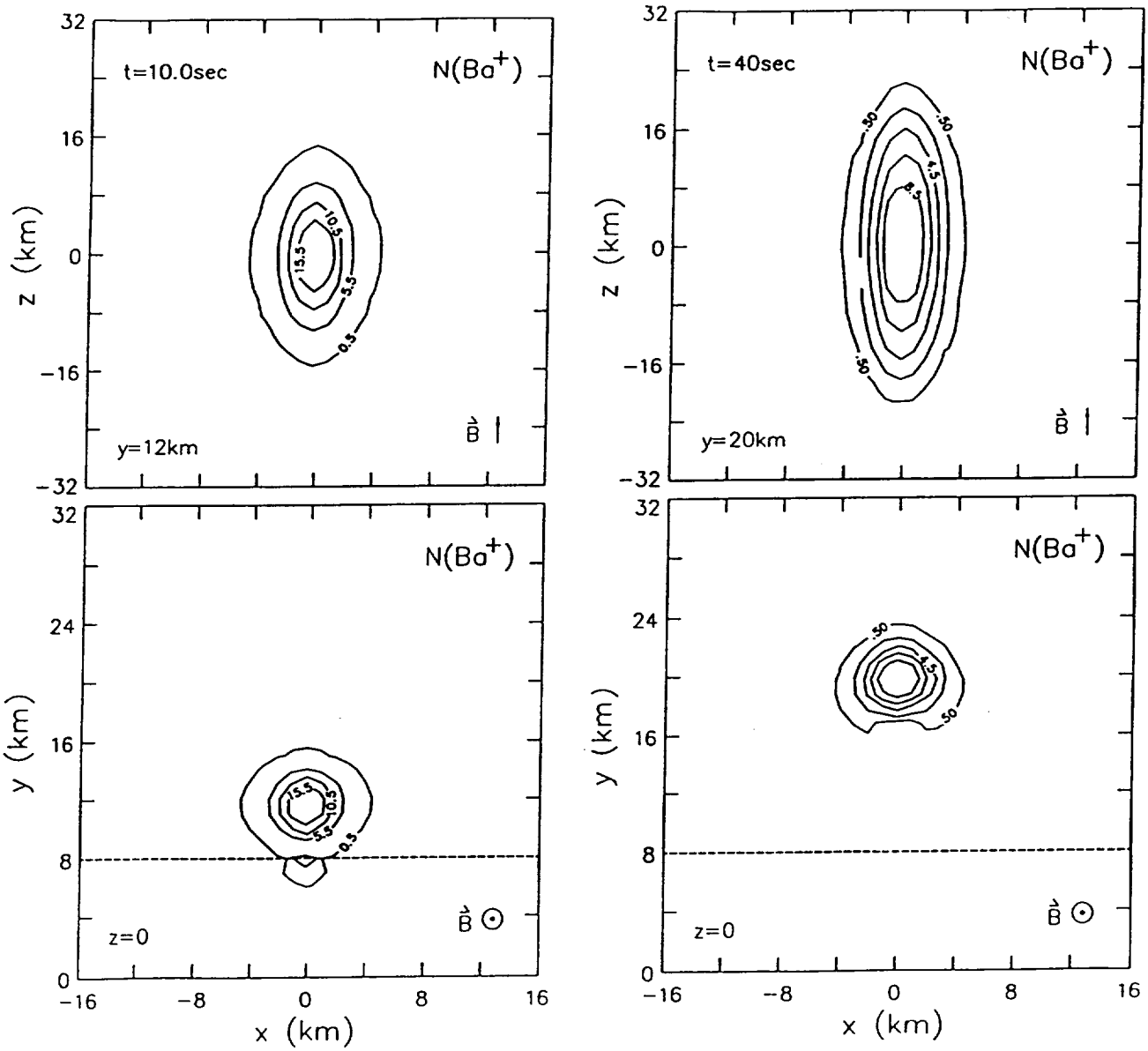
t=10.0sec
N(Ba+)
y=12km
B
z=0
t=40sec
y=20km
z (km)
y (km)
x (km)
32
16
0
−16
−32
24
8
−8
15.5
10.5
5.5
0.5
4.5
.50

Figure 3.

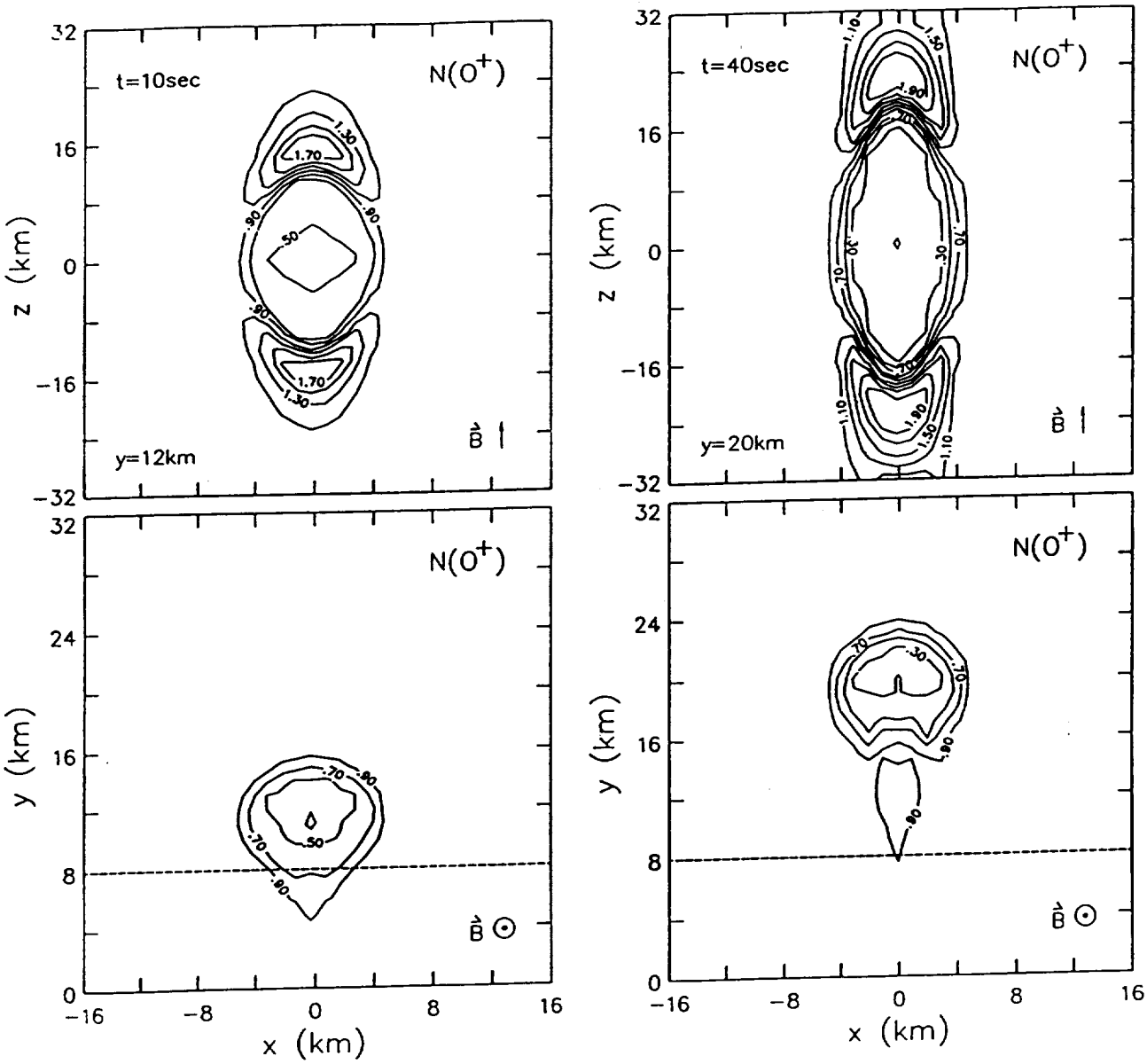
t=10sec
N(O+)
y=12km
B
z (km)
N(O+)
y (km)
x (km)
t=40sec
N(O+)
y=20km
B
z (km)
N(O+)
y (km)
x (km)

Figure 4.

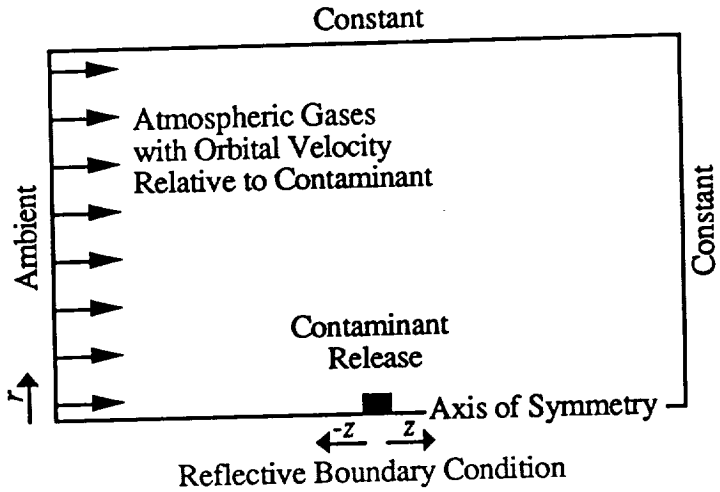
Constant
Atmospheric Gases
with Orbital Velocity
Relative to Contaminant
Ambient
Constant
Contaminant
Release
r
Axis of Symmetry
-z
z
Reflective Boundary Condition

Figure 5.

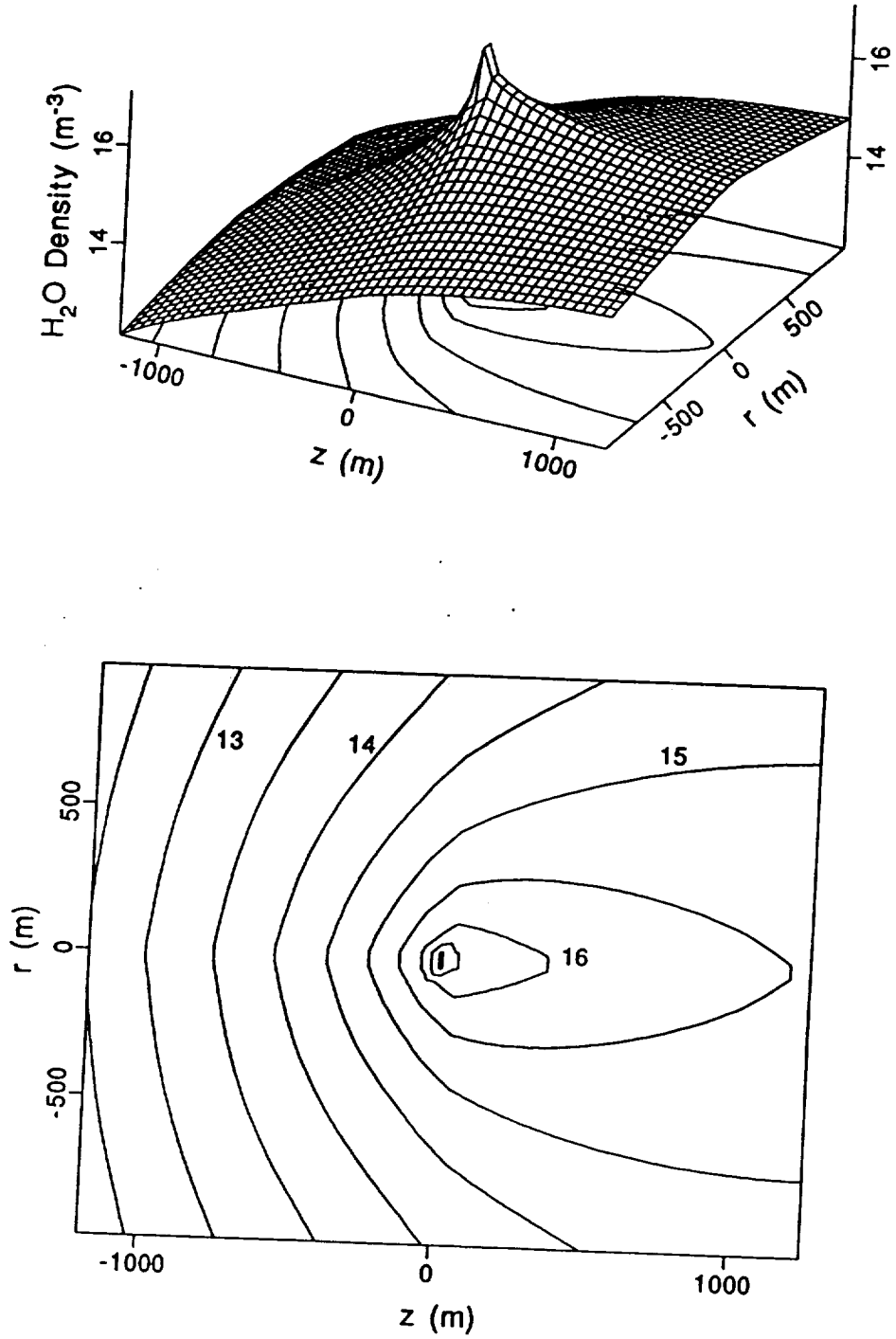
H2O Density (m-3)
16
14
-1000
0
1000
z (m)
-500
0
500
r (m)
16
14
13
14
15
16
500
0
-500
r (m)
-1000
0
1000
z (m)

Figure 6.

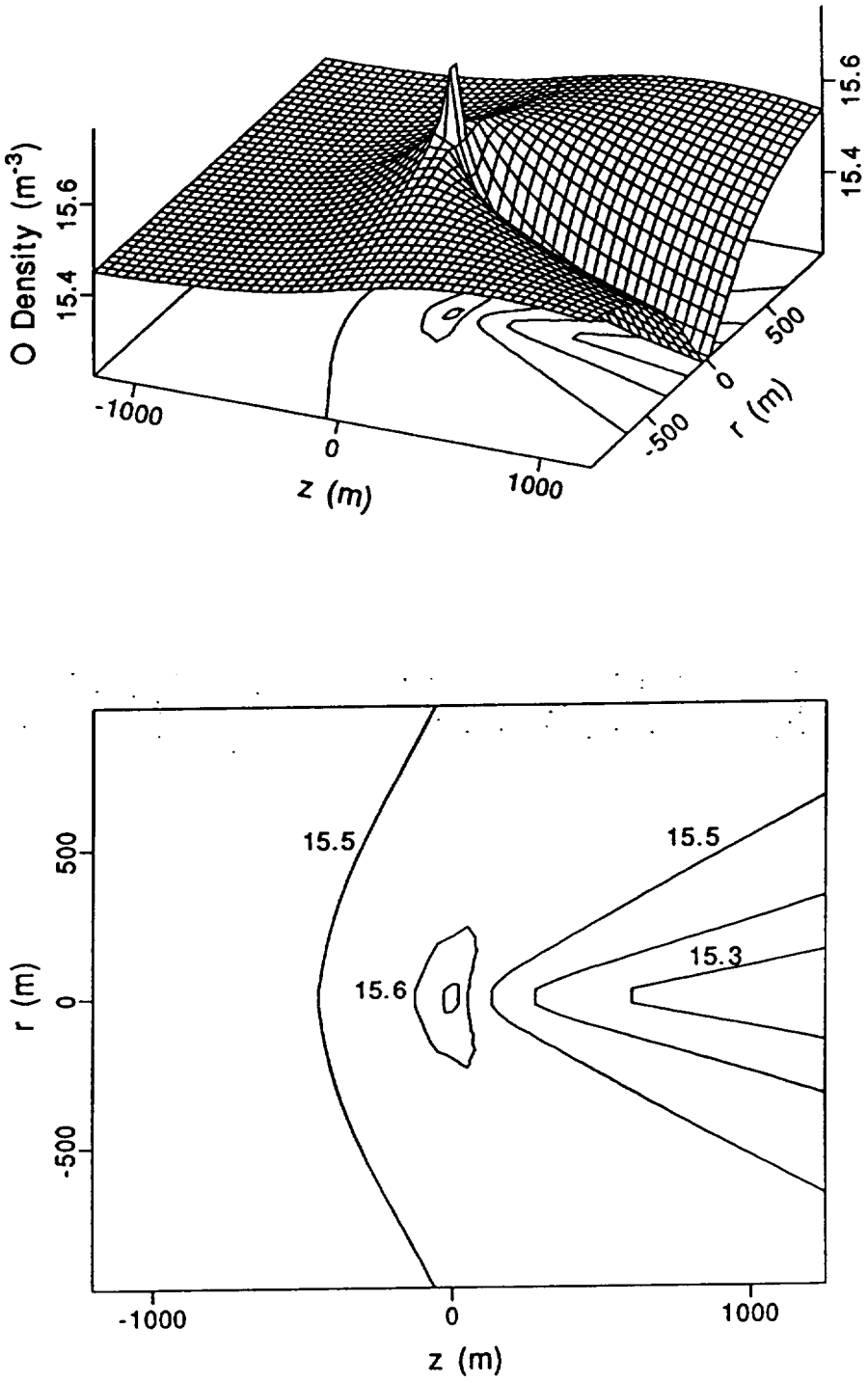
O Density (m-3)
15.4
15.6
-1000
0
1000
z (m)
-500
0
500
r (m)
15.4
15.6
15.5
15.5
15.6
15.3
r (m)
500
0
-500
-1000
0
1000
z (m)

Figure 7.

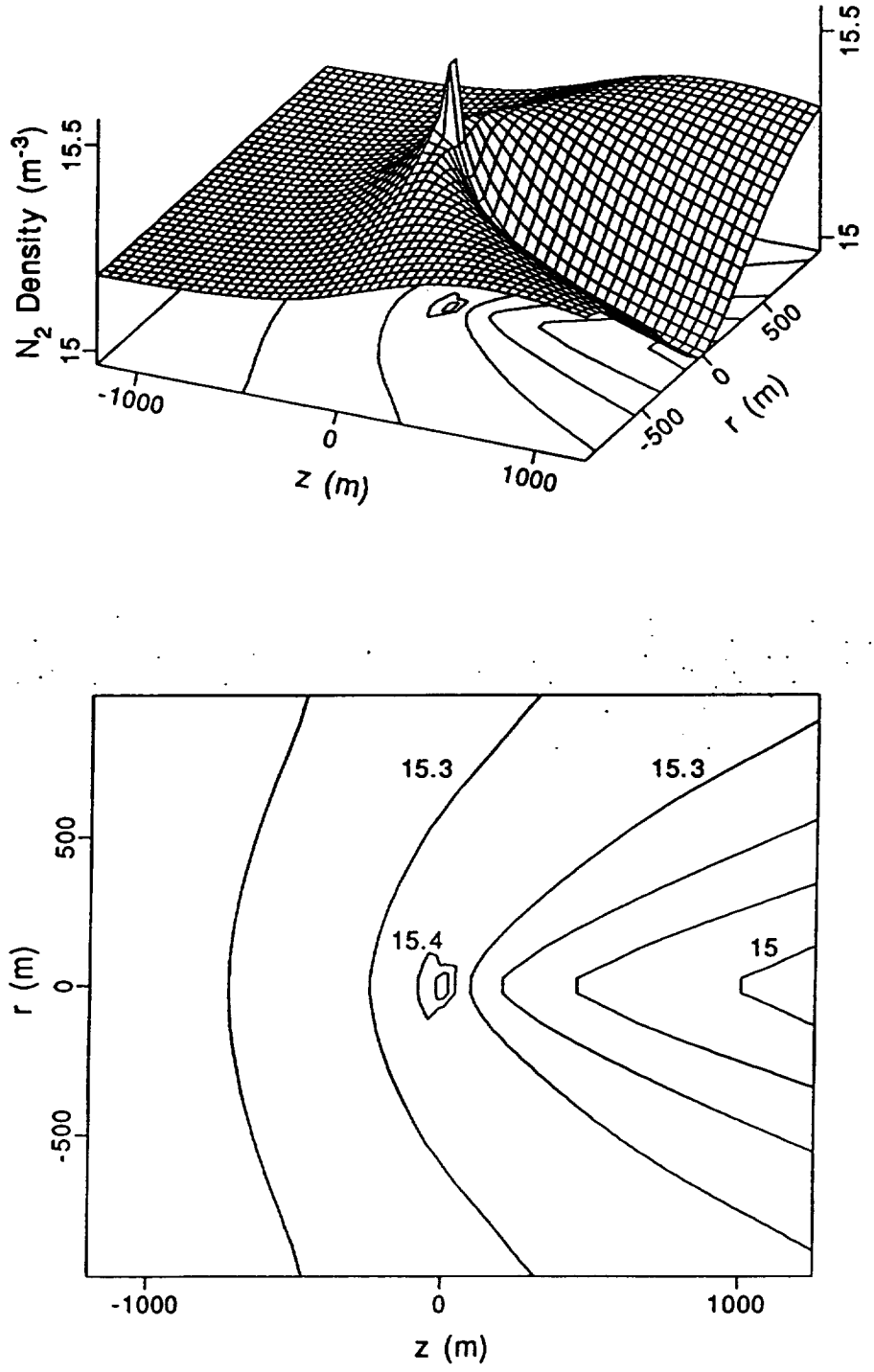
N2 Density (m-3)
15.5
15
-1000
0
1000
z (m)
-500
0
500
r (m)
15.5
15
15.3
15.3
15.4
15
500
0
-500
r (m)
-1000
0
1000
z (m)

Figure 8.

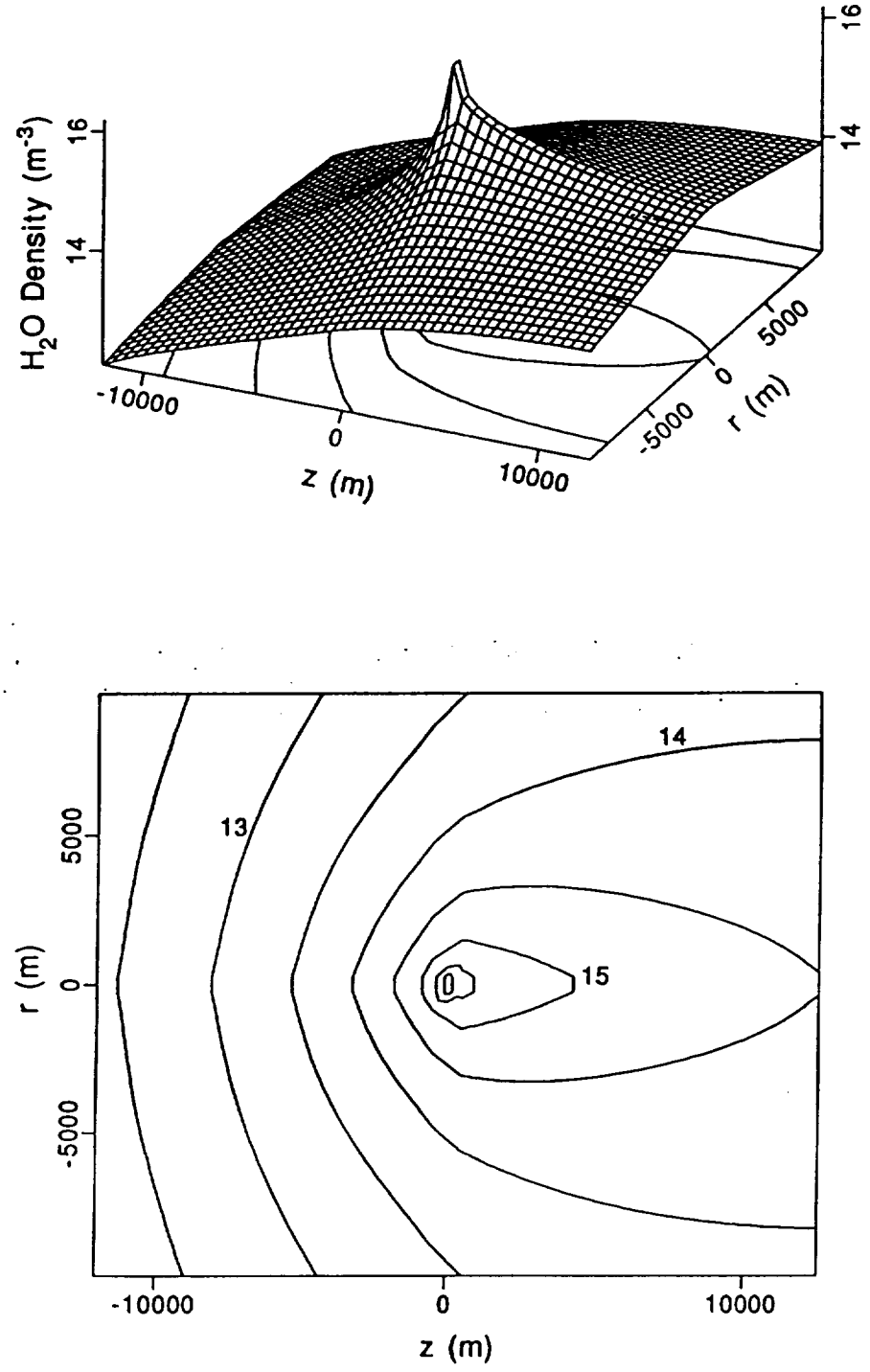
H2O Density (m-3)
16
14
-10000
0
10000
z (m)
16
14
5000
0
-5000
r (m)
14
13
15
5000
0
-5000
r (m)
-10000
0
10000
z (m)

Figure 9.

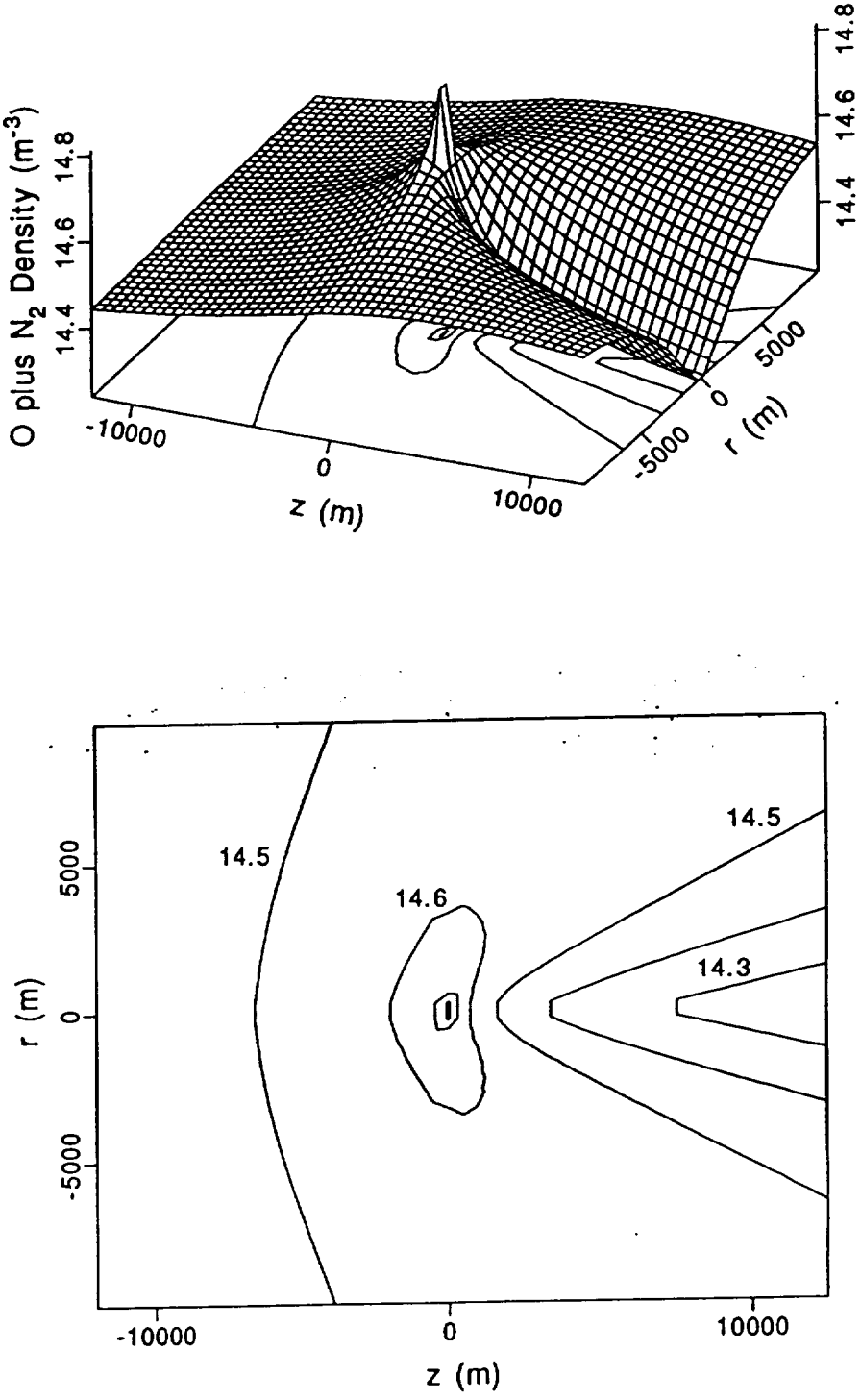
O plus N_2 Density (m^{-3})
14.4
14.6
14.8
-10000
0
10000
z (m)
-5000
0
5000
r (m)
14.4
14.6
14.8
14.5
14.5
14.6
14.3
5000
0
-5000
r (m)
-10000
0
10000
z (m)

Figure 10.

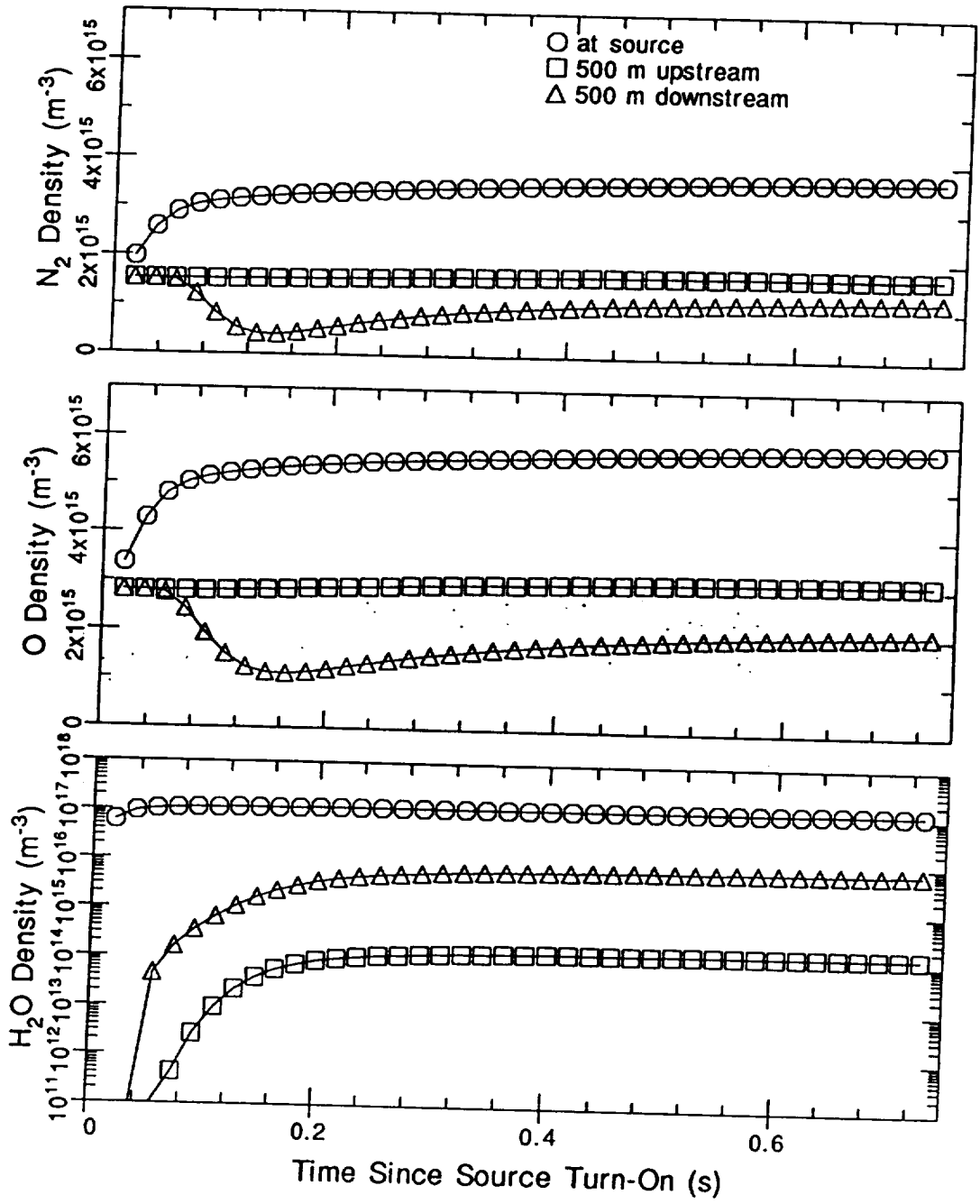
at source
500 m upstream
500 m downstream
N2 Density (m-3)
O Density (m-3)
H2O Density (m-3)
Time Since Source Turn-On (s)

Figure 11.

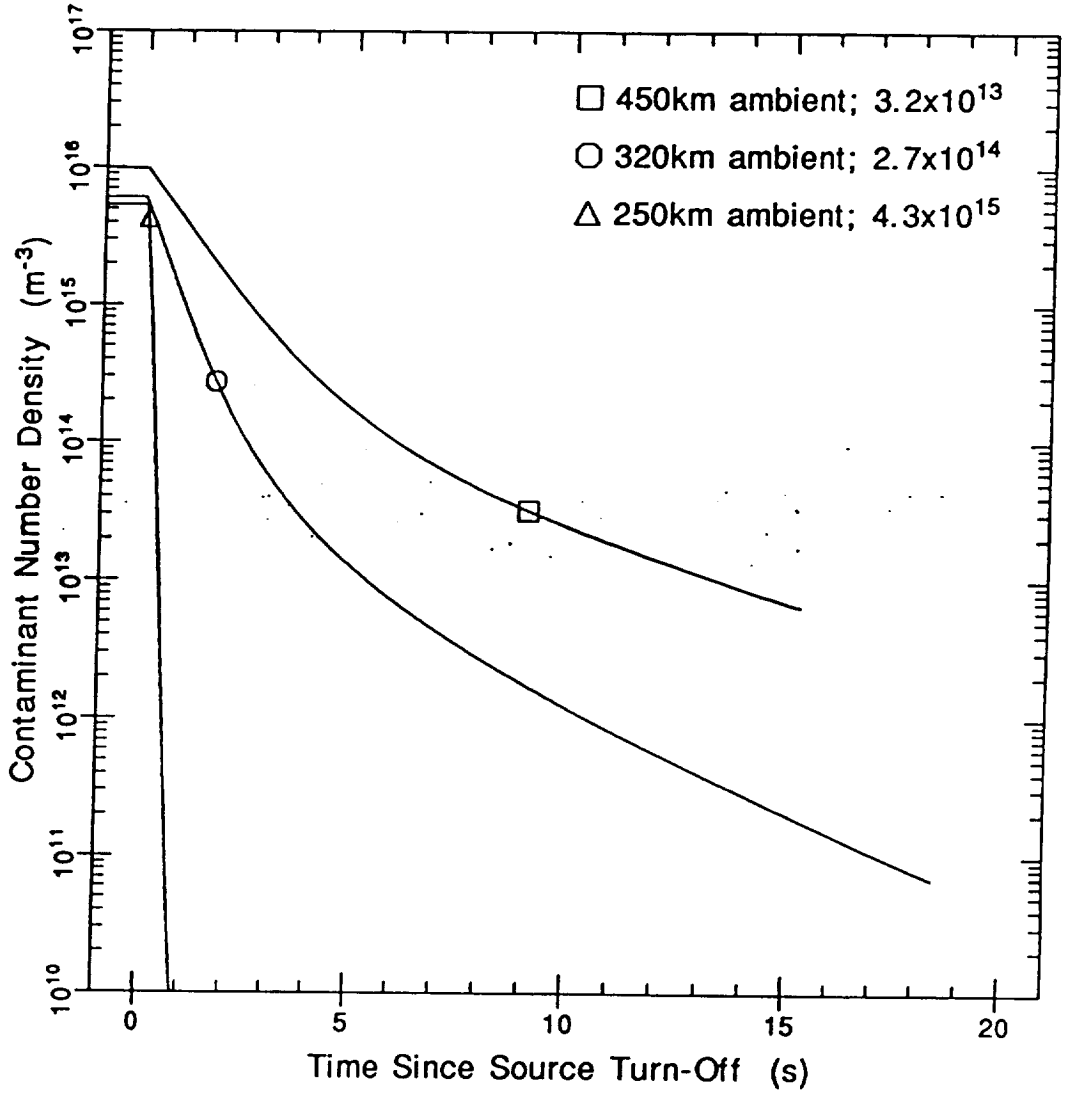
□ 450km ambient; 3.2x10^13
○ 320km ambient; 2.7x10^14
△ 250km ambient; 4.3x10^15
Contaminant Number Density (m^-3)
10^17
10^16
10^15
10^14
10^13
10^12
10^11
10^10
0
5
10
15
20
Time Since Source Turn-Off (s)

Figure 12.

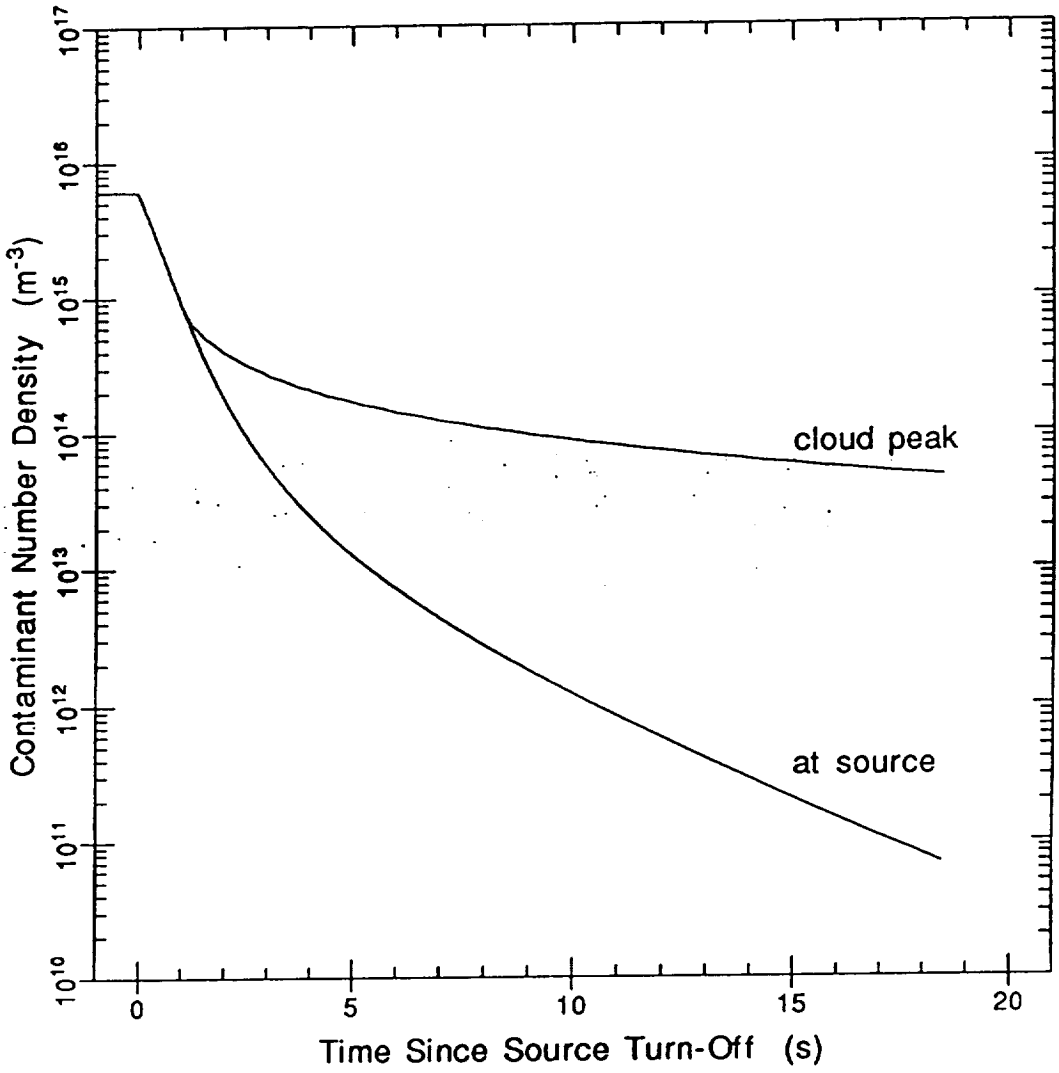
Contaminant Number Density (m^{-3})
10^{17}
10^{16}
10^{15}
10^{14}
10^{13}
10^{12}
10^{11}
10^{10}
cloud peak
at source
0
5
10
15
20
Time Since Source Turn-Off (s)

Figure 13.

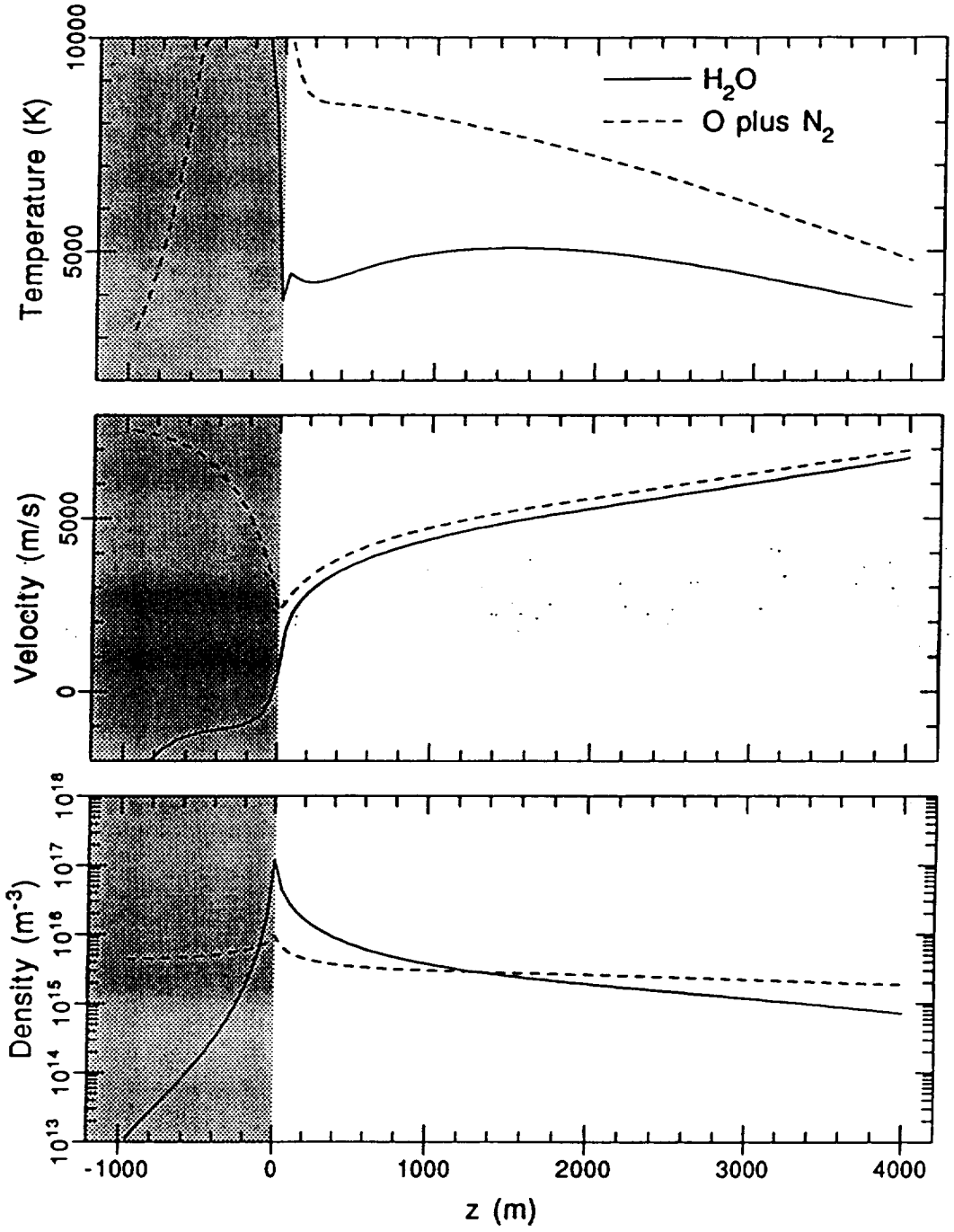
Temperature (K)
10000
5000
H2O
O plus N2
Velocity (m/s)
5000
0
Density (m-3)
10^18
10^17
10^16
10^15
10^14
10^13
-1000
0
1000
2000
3000
4000
z (m)

Figure 14.

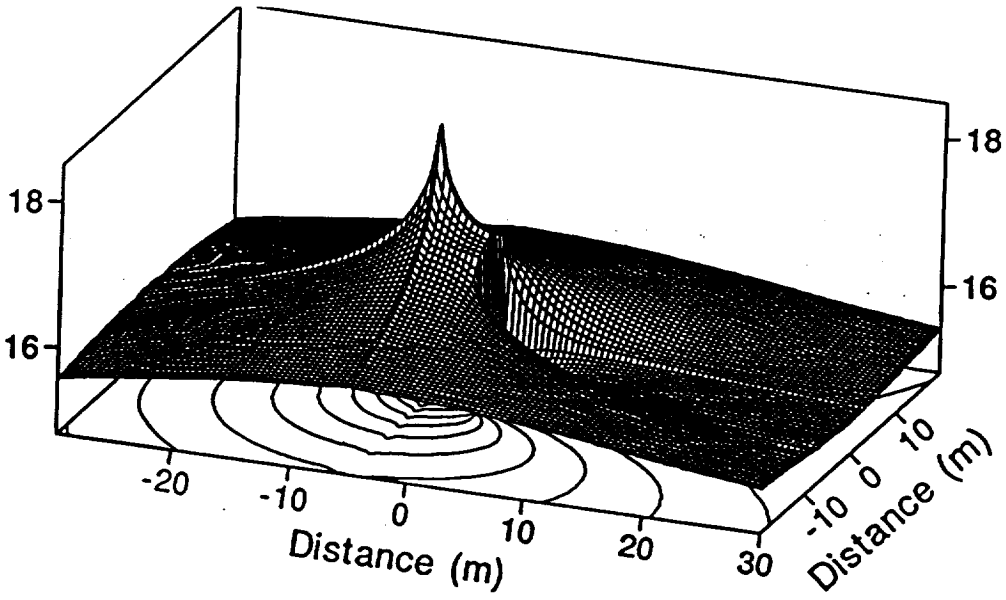

Figure 15.

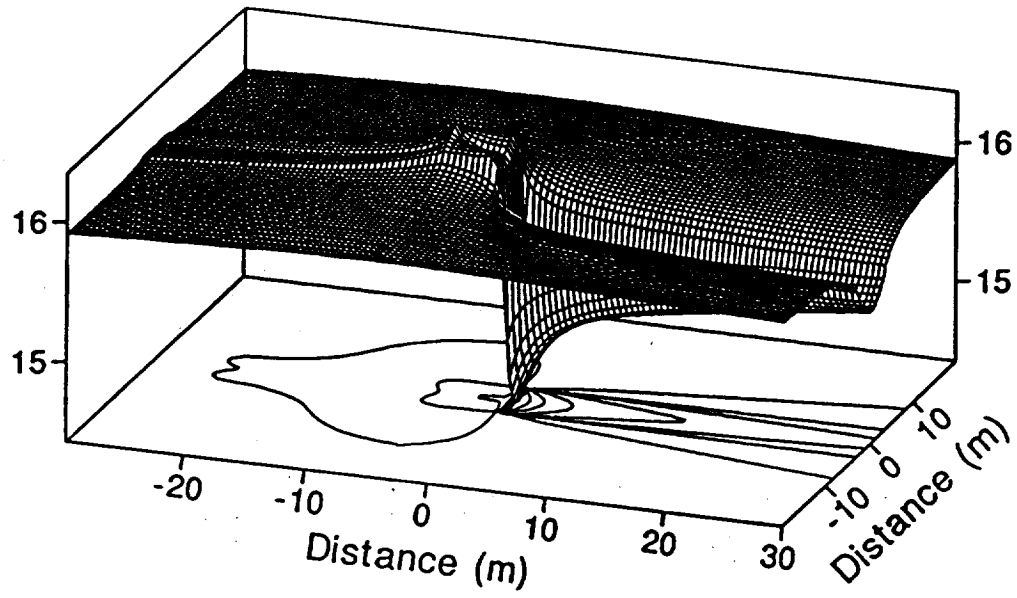

Figure 16.

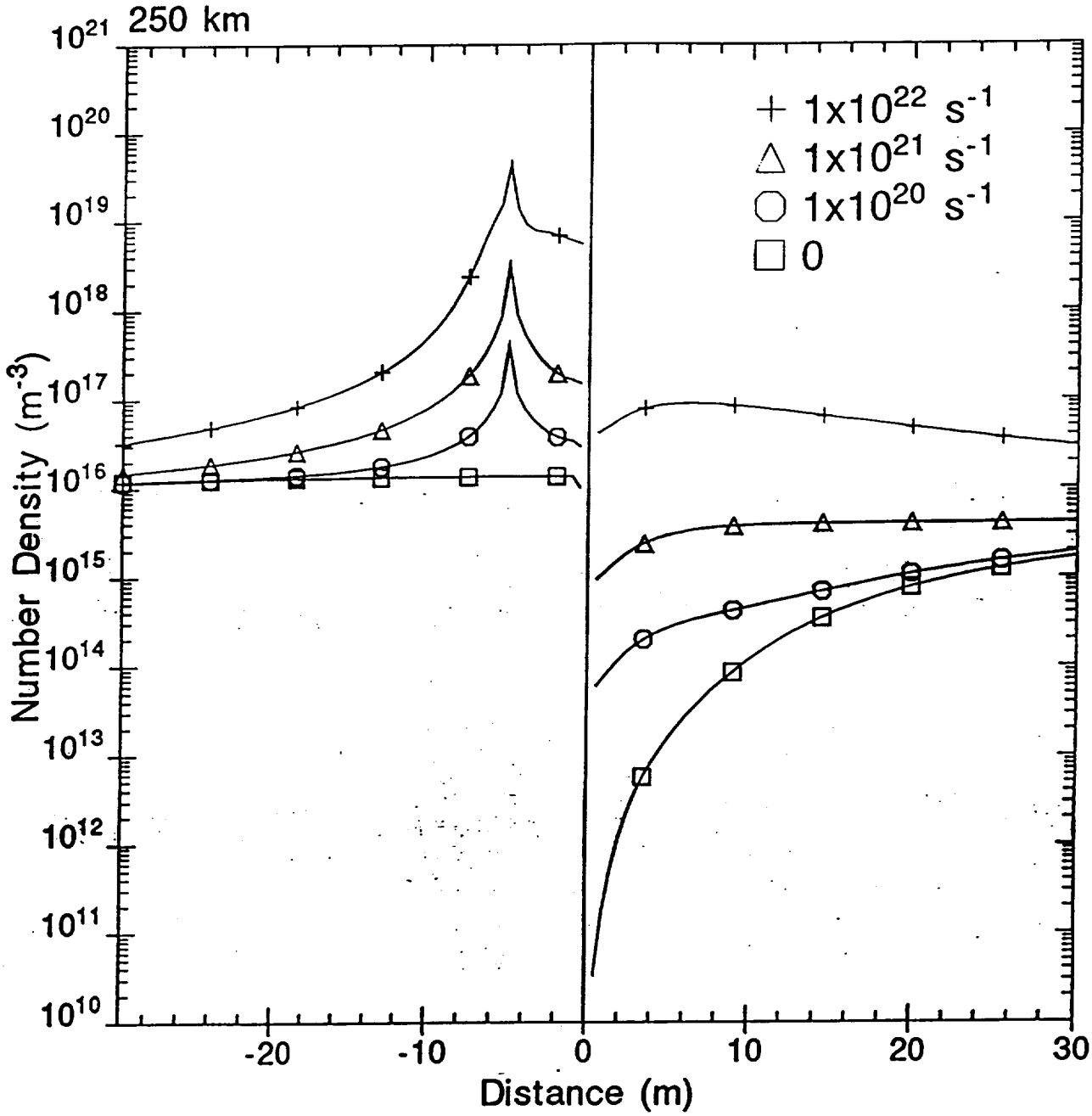
250 km
10^{21}
10^{20}
10^{19}
10^{18}
10^{17}
10^{16}
10^{15}
10^{14}
10^{13}
10^{12}
10^{11}
10^{10}
Number Density (m^{-3})
+ $1x10^{22}$ s^{-1}
△ $1x10^{21}$ s^{-1}
○ $1x10^{20}$ s^{-1}
□ 0
-20
-10
0
10
20
30
Distance (m)

Figure 17.

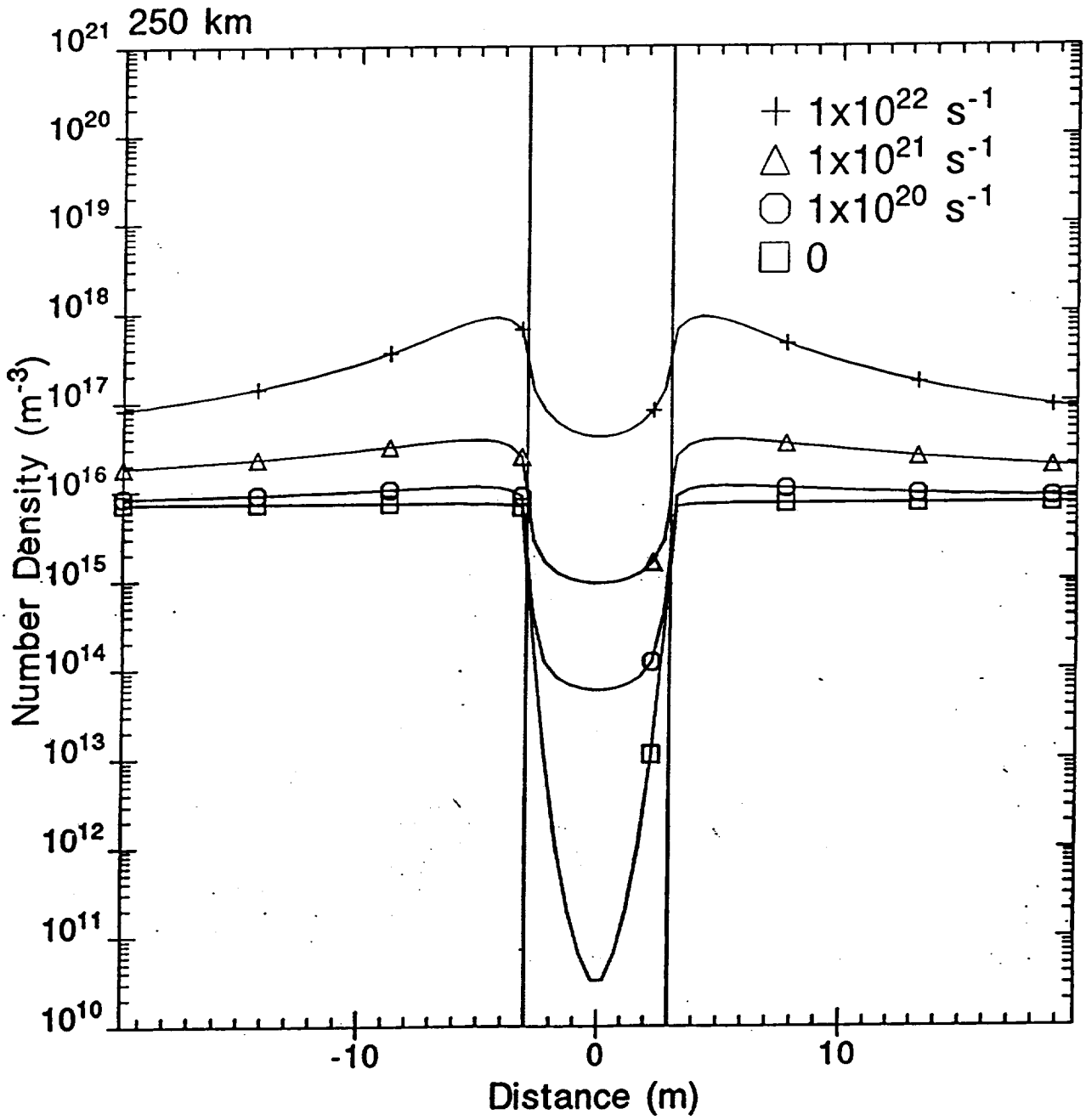
250 km
10^{21}
10^{20}
10^{19}
10^{18}
10^{17}
10^{16}
10^{15}
10^{14}
10^{13}
10^{12}
10^{11}
10^{10}
Number Density (m^{-3})
+ $1x10^{22}$ s^{-1}
△ $1x10^{21}$ s^{-1}
○ $1x10^{20}$ s^{-1}
□ 0
-10
0
10
Distance (m)

Figure 18.

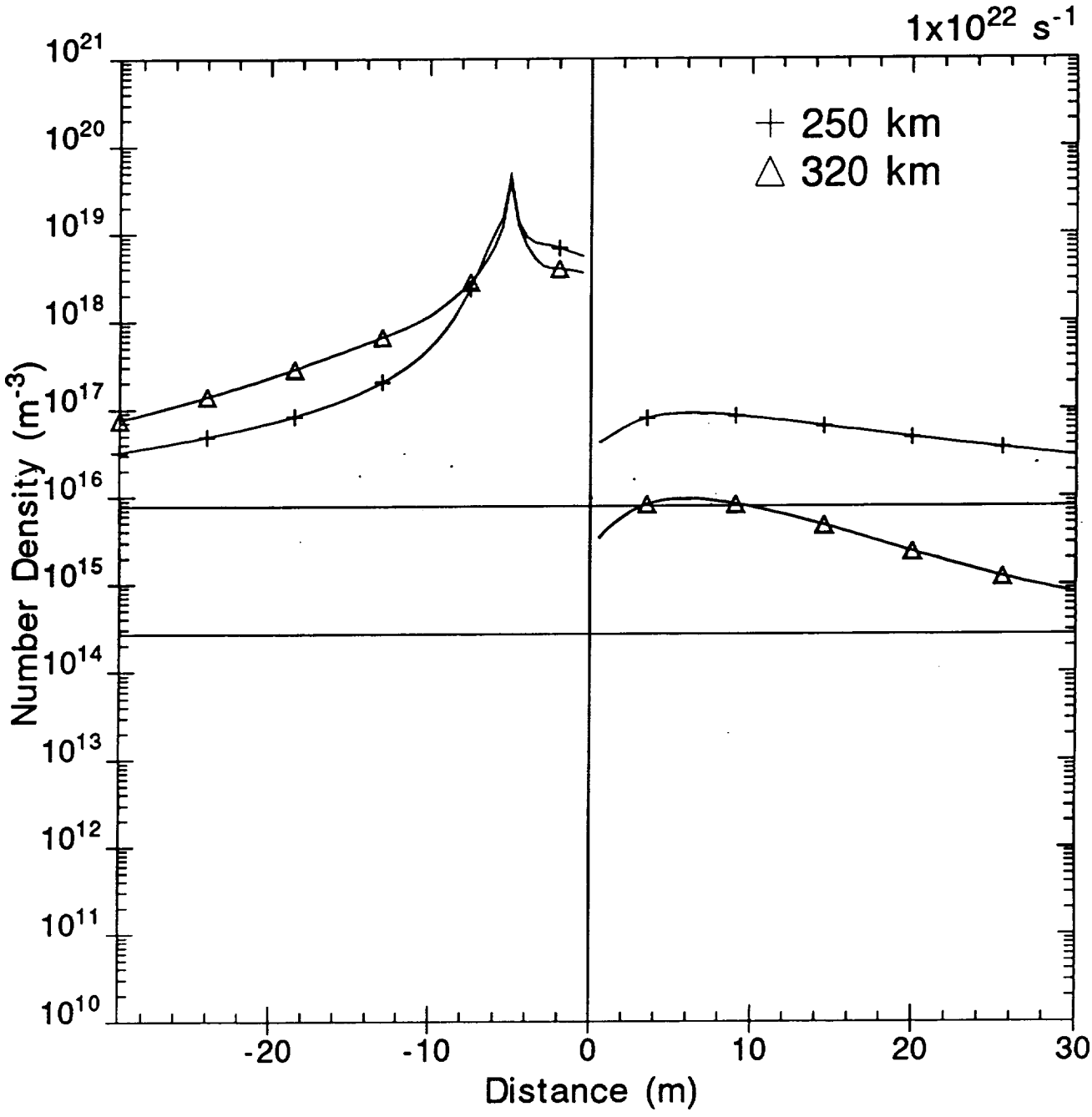
1x10^22 s^-1
+ 250 km
△ 320 km
Number Density (m^-3)
10^21
10^20
10^19
10^18
10^17
10^16
10^15
10^14
10^13
10^12
10^11
10^10
-20
-10
0
10
20
30
Distance (m)

Figure 19.

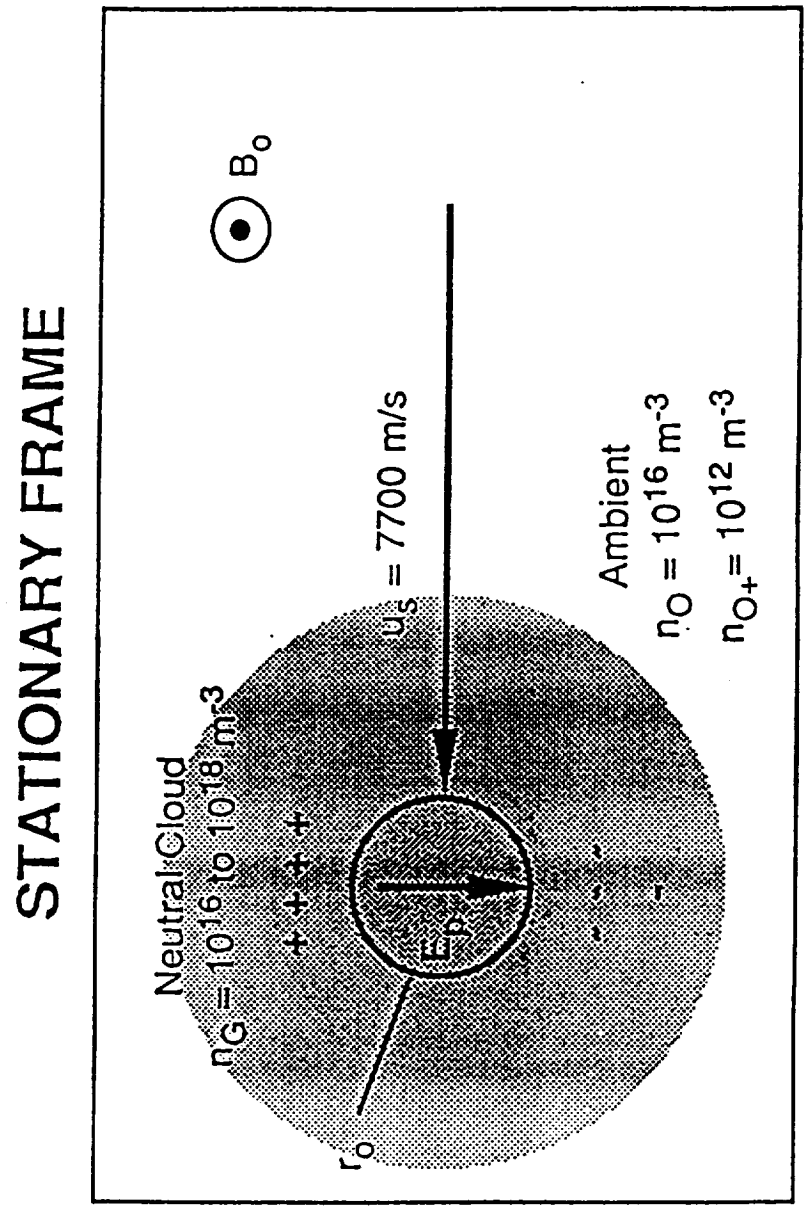
STATIONARY FRAME
B_o
u_s = 7700 m/s
Ambient
$n_O = 10^{16}$ m^{-3}
$n_{O+} = 10^{12}$ m^{-3}
Neutral Cloud
$n_G = 10^{16}$ to 10^{18} m^{-3}
E_p
r_o

Figure 20.

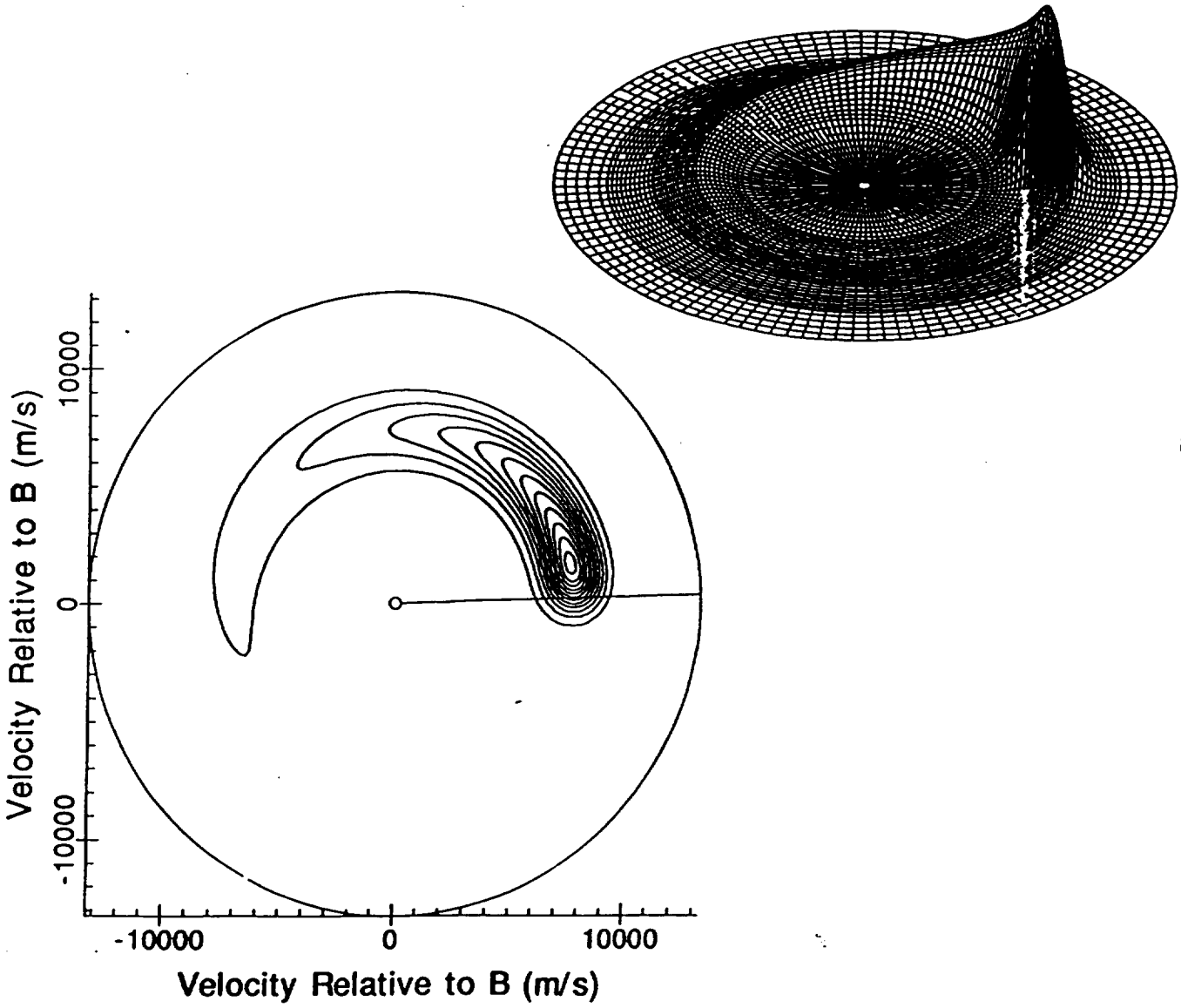
Velocity Relative to B (m/s)
10000
0
-10000
-10000
0
10000
Velocity Relative to B (m/s)

Figure 21.

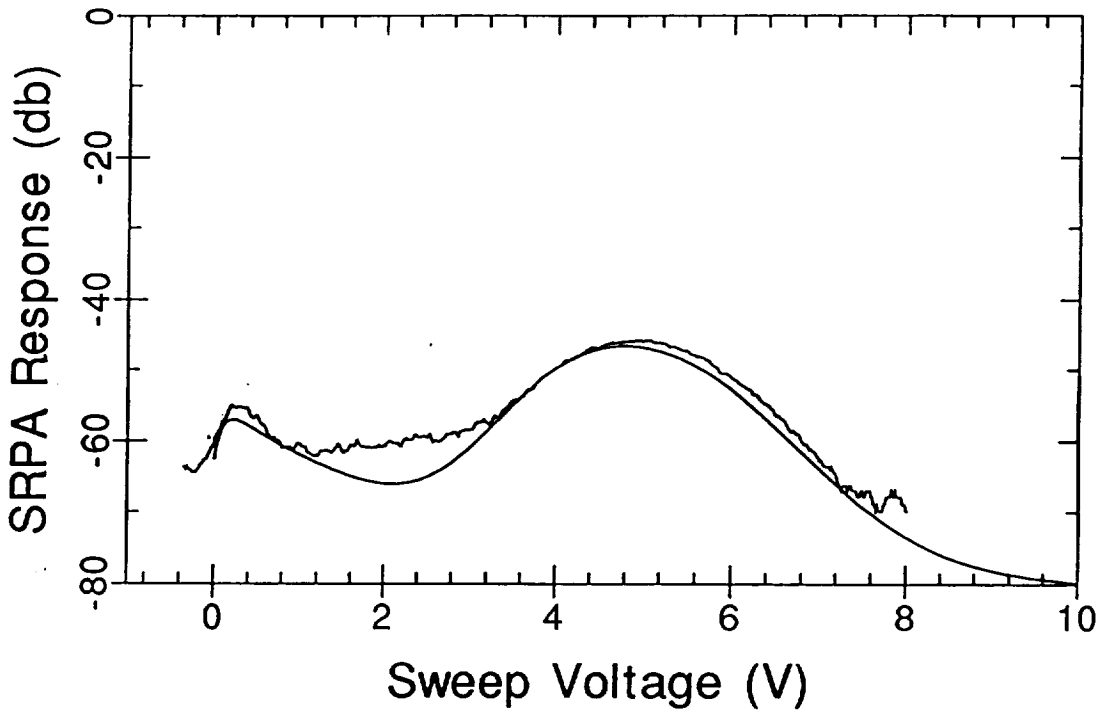

Figure 22.